Magmatic Enclaves and Andesitic Lavas from Mt. Lamington, Papua New Guinea: Implications for Recycling of Earlier-fractionated Minerals through Magma Recharge

J. ZHANG[1]*, J. P. DAVIDSON[1], M. C. S. HUMPHREYS[1], C. G. MACPHERSON[1], I. NEILL[1,2]

[1]DEPARTMENT OF EARTH SCIENCES, UNIVERSITY OF DURHAM, DURHAM, DH1 3LE, UK

[2]SCHOOL OF GEOGRAPHICAL AND EARTH SCIENCES, UNIVERSITY OF GLASGOW, GLASGOW, G12 8QQ, UK

*Corresponding author. E-mail: jing.zhang5@durham.ac.uk

ABSTRACT

Mt. Lamington is a composite, dome-forming volcano in Papua New Guinea, sitting on the Papuan Ultramafic Belt (PUB) ophiolite. The 1951 eruption produced andesitic dome lavas with numerous basaltic-andesitic enclaves and a few PUB ultramafic xenoliths. To understand the nature of the 1951 eruption, and to assess the effect of assimilating ophiolitic crust in modifying the geochemistry of arc magmas, we carried out petrological, mineralogical and geochemical studies on andesitic lavas as well as magmatic enclaves and ultramafic inclusions. The mineralogy of the enclaves is dominated by amphibole and plagioclase, similar to the andesitic lava hosts. The textures of the enclaves vary from fine-grained diktytaxitic to coarser-grained plutonic textured. We interpret this variation to result from variable cooling rates in the enclave-forming magma body when it invades the overlying andesite. The diktytaxitic enclaves contain variable proportions of host-derived amph+plag antecrysts and xenocrysts of ol+sp±cpx±amph with disequilibrium textures, indicating interaction with host lava and assimilation of foreign materials, respectively. A previous study argued that the olivine xenocrysts with chromian spinel inclusions are derived from the PUB, and thus that the PUB contaminated the Mt. Lamington magmas. We demonstrate that this is highly unlikely on the basis of morphological and compositional discrepancies between PUB ol+sp, sampled in nodules, and the xenocrysts. Mass balance indicates that the high whole-rock Ni contents of enclaves and andesitic hosts can be explained by olivine incorporation and do not require any PUB involvement. The olivines are considered to represent crystal mush fractionated from precursor(s) of andesitic and/or pre-1951 shoshonitic lavas. Their presence in enclaves represents recycling of earlier-fractionated components through magma recharge. We argue that this recycling is an important and underestimated process in shaping arc magmas.

KEY WORDS: assimilation; magmatic enclaves; magma recharge; Mt. Lamington; ophiolite contamination; Papuan Ultramafic Belt

INTRODUCTION

Volcanism on the Papuan Peninsula is of particular interest because it represents arc-like magmatism decoupled from active subduction (Jakeš & Smith, 1970; Johnson *et al.*, 1978; Smith *et al.*, 1979; Smith, 1982; Smith & Compston, 1982; Arculus *et al.*, 1983; Smith & Milsom, 1984; Smith, 2013a). The most recent volcanic activity on the Papuan peninsula was represented by the 1951 eruption of Mt. Lamington, Papua New Guinea (PNG). The eruption initiated on 21st January 1951; this climactic phase, followed by another 8 major explosive episodes which lasted until 5th March, 1951, resulted in the devastation of an area > 100 km^2, as well as around 3000 deaths (Taylor, 1958). Prior to this eruption, Mt. Lamington had never been regarded as a volcano, due to a lack of observations or eruption records. A lava dome was constructed intermittently within the craters during and after the explosive eruptions. In 1956, the dome approximated a truncated cone with an estimated size of ~550 m in height and ~1300 m and ~600 m in width at the base and summit, respectively (Taylor, 1958; Arculus *et al.*, 1983), representing a volume of about 0.4 km^3. The dome sits on older volcanic products of shoshonitic composition (pre-1951 shoshonite, unknown age). It comprises andesitic lavas (1951 andesite) and contains abundant mafic-intermediate magmatic enclaves, as well as ultramafic xenoliths (Taylor, 1958; Arculus *et al.*, 1983). The 1951 andesite and the enclaves are characterized by high Cr and Ni contents, and enrichment in incompatible elements relative to volcanism at the adjacent New Britain arc (Arculus *et al.*, 1983). The high concentrations of Cr and Ni were previously ascribed to assimilation of ultramafic material that is found in PNG and thought to underlie Mt. Lamington (Papuan Ultramafic Belt, PUB; Arculus *et al.*, 1983), but this hypothesis cannot also explain the high incompatible element concentrations; the heat budget required to assimilate such refractory material is also problematic.

In order to investigate further the nature of volcanism on the Papuan Peninsula and to understand potential compositional variations in the magma source region and in the magmatic processes which occurred at crustal levels, we obtained new trace element element and Nd-Sr isotope whole-rock and mineral composition data for the andesites and magmatic enclaves produced during the 1951 eruption of Mt. Lamington. We link these new data with petrographic observations to bring additional insights on the inter-relationships between the 1951 andesite and its magmatic and ultramafic inclusions.

TECTONIC AND GEOLOGICAL SETTING

Mt. Lamington (8º57'S, 148º09'E) is a Quaternary composite volcano located on the Papuan Peninsula, together with other dormant edifices: Hydrographers Range, Mt. Victory and Mt. Trafalgar. The Papuan Peninsula occurs in a tectonically complex boundary region where the north-northeast moving Australian Plate converges with the westward moving Pacific Plate (Baldwin *et al.*, 2012, Davies, 2012; Fig. 1a). The Papuan Peninsula lies on the Australian Plate which is actively subducting beneath the Pacific Plate at the New Britain Arc and the Solomon Arc (Baldwin *et al.*, 2012). To the east of the Papuan Peninsula, seafloor spreading in the Woodlark Sea Basin started ~3.5 Ma ago and has been propagating westward (Taylor *et al.*, 1995; Taylor *et al.*, 1999), probably resulting from slab pull owing to the subduction of the Solomon Sea Plate (Weissel *et al.*, 1982). The Pocklington Trough to the south of the Papuan Peninsula represents a former continental passive margin formed as a result of the Coral Sea Basin opening in the Middle-Late Eocene (Davies & Smith, 1971, Smith & Milsom, 1984). To the north of the Papuan Peninsula, the Trobriand Trough is the trench of a south-dipping subduction zone. The absence of a seismically-defined Benioff Zone (Hall & Spakman, 2002; Wallace *et al.*, 2004), suggests that subduction is presently inactive, although it might have been active in the Miocene (Hill & Raza, 1999). Current magmatism on the Papuan Peninsula is speculated to be a product of delayed partial melting of subduction-modified mantle (Johnson *et al.*, 1978; Arculus *et al.*, 1983), triggered by upwelling asthenospheric mantle as a result of westward propagation of the Woodlark Spreading-Rifting System (Smith, 2013a).

The Papuan Peninsula contains (Fig. 1b; Davies, 2012; Smith, 2013b): (1) Quaternary composite volcanoes and sedimentary deposits (including Mt. Lamington); (2) the Papuan Ultramafic Belt (PUB; see below); (3) the Owen Stanley Metamorphic Complex, composed of the largely metasedimentary Kagi Metamorphics and the largely metabasic Emo Metamorphics (see below); (4) the Aure Fold Belt, a westward-facing thrust and fold belt composed of thick Late Oligocene-Pliocene clastic-dominated sediments; and (5) the Milne Terrane, made up of Cretaceous-Eocene MORB-like basalts, interpreted as the northern margin of the uplifted Coral Sea Basin.

The Mt. Lamington and Hydrographers Range volcanic edifices sit on a basement of PUB and Emo Metamorphics (Taylor, 1958; Arculus *et al.*, 1983). The PUB comprises obducted Late Cretaceous oceanic crust (ophiolite) lying above the Owen Stanley

Metamorphic Complex; the emplacement of the PUB is thought to have taken place in the Eocene (Davies & Smith, 1971; Davies & Jaques, 1984; Lus *et al.*, 2004). From bottom to top, the PUB comprises three layers: ultramafic rocks (thickness of 4-8 km), gabbro (~4 km) and basalt (4-6 km; Davies & Smith, 1971). The ultramafic section is predominantly harzburgitic tectonite with olivine ($Fo_{91.6-93.6}$), orthopyroxene ($En_{92.1-93.4}$) and chromian spinel (Cr/Cr+Al = 0.9), as well as peridotite containing olivine ($Fo_{89.3}$), diopside, accessory chromian spinel (Cr/Cr+Al = 0.7), poikilitic orthopyroxene (En_{84}), and rare anorthitic plagioclase (An_{81-86}; Davies & Smith, 1971; England & Davies, 1973; Jaques & Chappell, 1980). The gabbro section varies from olivine-rich gabbro at the base to olivine-poor norite-gabbro at the top, with cumulus olivine ($Fo_{80.6}$), plagioclase (An_{81-93}) and poikilitic augite/hypersthene (Davies & Smith, 1971; England & Davies, 1973; Jaques & Chappell, 1980). The basalt section is mainly composed of aphanitic pillow lavas, with rare microphenocrysts of Fe-rich augite ($En_{40-21}Wo_{35-48}Fs_{25-31}$) or labradorite (Davies & Smith, 1971; England & Davies, 1973; Jaques & Chappell, 1980). The geochemistry of the basalts (SiO_2 = 47-50 wt %) is characterized by high Fe (FeO_{tot} = 14-15 wt %) and a MORB-like trace element signature (Davies & Smith, 1971; England & Davies, 1973; Jaques & Chappell, 1980).

The Emo Metamorphics that underlie Mt. Lamington and the PUB are composed of tholeiitic greenschist, amphibolite, and lawsonite/garnet blueschist thrust sheets (Worthing & Crawford, 1996). The geochemistry varies from occasional LREE-depleted N-MORB with Zr/Nb > 40, to more dominant LREE-enriched E-MORB with Zr/Nb of 8-16. $^{143}Nd/^{144}Nd$ displays a large variation from 0.512744±13 in garnet-bearing blueschists to 0.513107±18 in amphibolites (Worthing & Crawford, 1996).

ANALYTICAL METHODS

The samples used in this study are those described by Arculus *et al.* (1983). The major element data (XRF) from Arculus *et al.* (1983) are re-evaluated together with new trace element and isotopic data collected for this study.

For trace element analysis sample powders from the Arculus *et al*. (1983) study were dissolved using a routine HF-HNO_3 digestion procedure (Ottley *et al.*, 2003) and analysed on a Thermo Scientific X Series 2 inductively coupled plasma mass spectrometer (ICP-MS) at the Durham Geochemistry Centre, Durham University. Monitoring of instrumental

performance was achieved by sample-standard-blank bracketing using procedural blanks (n=15) and international reference standards W2 (n=8), BHVO-1 (n=4), AGV-1 (n=4), NBS688 (n=4), and BE-N (n=4), with Re-Rh spike solutions. Two Mt. Lamington sample duplicates (a shoshonite, LAM-27D and an andesite, LAM-14) were used as internal standards. Repetitive runs of W2 across two batches of analysis typically gave relative standard deviations (%RSD) of rare earth element (REE) analyses of <3.5%, with transition metal, large ion lithophile (LILE) and high field strength element (HFSE) analyses giving RSDs of <9% (Table 1). ICP-MS analyses of the Mt. Lamington samples agree very well with the XRF data (Arculus *et al.*, 1983), except that V concentrations are slightly higher and Zr concentrations are lower by 30-80% relative to the XRF data (Supplementary Data Appendix Fig. 1). For Zr, ICP-MS analyses reproduce reference standards very well, however they failed to reproduce Zr by multiple analysis of an internal rock standard (LAM-27D) within and between batches of measurements, and the XRF data. Therefore, we believe this discrepancy is due to incomplete dissolution of accessory minerals such as zircon during our sample preparation. Considering that zircon is one of the most important host of Hf, the concentrations of Hf should also be biased by this effect. Thus, the original XRF Zr data from Arculus *et al.* (1983) are used instead and Hf data are not considered. Ta data are not reported since the rock samples were prepared in a tungsten carbide mill.

For whole-rock Sr-Nd isotopes, sample powders were dissolved in Teflon beakers using HF-HNO_3 solution and analysed on a thermal ionization mass spectrometer at the University of California, Los Angeles. Sr and Nd separation followed standard cation exchange techniques (e.g., Richard *et al.*, 1976). Sr isotope ratios were determined using a VG Sector multicollecting mass spectrometer in dynamic mode. Nd isotopic ratios were measured on a VG Sector 54-30 multicollecting mass spectrometer in static mode. Total process Sr and Nd blanks are ~350 pg and ~100 pg, respectively. Duplicate analyses of the international reference standard NBS987 gave $^{87}Sr/^{86}Sr = 0.710248 \pm 17$ (n=5) and the La Jolla standard gave an average $^{143}Nd/^{144}Nd$ of 0.511840 ± 11 (n=4; Davidson *et al.*, 1993). The full dataset of bulk-rock geochemistry is given in Table 1.

For backscattered electron (BSE) imaging and electron probe microanalysis (EPMA), the samples were prepared as standard polished probe sections and carbon-coated to a thickness of 25 nm. BSE images were collected with a Hitachi SU-70 FEG scanning electron microscope at Durham University. EPMA was carried out at Edinburgh University, using a Cameca SX100 electron microprobe equipped with 5 wavelength-dispersive spectrometers.

Minerals were analysed using a 15 kV accelerating voltage, with 4-10 nA beam current for major elements and 100 nA for trace elements. A PAP correction procedure was applied to all analyses. Anhydrous minerals (plagioclase, olivine, orthopyroxene, clinopyroxene and oxides) were analysed using a 2-5 μm spot; for hydrous minerals (amphibole and biotite) a 10 μm defocused beam was used. Glasses were analysed using a 15 kV accelerating voltage, 4 nA for major elements, 80 nA for minor elements and a 12 μm defocused beam. Calibration was undertaken using the following standards: wollastonite (Si, Ca), spinel (Al, Mg), fayalite (Fe), jadeite (Na), orthoclase (K), rutile (Ti), celestite (Sr), pure metal (Mn, Cr, Ni), NaCl (Cl) and synthetic $RbMnF_3$ (F). Representative EPMA data with typical 1 σ analytical errors are given in Tables 3-9; the full dataset is included in the Supplementary Data.

RESULTS

Petrology

1951 andesite

The dome lavas are a vesicular, porphyritic andesite with 56-64% phenocrysts/antecrysts of plagioclase (30-37%), amphibole (18-26%), biotite (1-2%), Fe-Ti oxides (1-3%) and rare clinopyroxene and orthopyroxene (point counting results, Table 2). Plagioclase phenocrysts/antecrysts are large and euhedral (typically 2.5–3 mm), with abundant inclusions of amphibole, biotite, oxides and apatite, as well as melt inclusions. Three types of plagioclase are distinguished based on the textures: i) oscillatory zoned, ii) patchy-zoned with oscillatory overgrowth rims, and iii) sieve-textured grains with oscillatory cores (Fig. 2a-c). Amphibole phenocrysts/antecrysts, typically 1.0-1.5 mm, are euhedral and fresh, without any evidence of breakdown. They contain abundant inclusions of plagioclase, Fe-Ti oxides, biotite and vesicle-bearing glass. Pleochroism varies from light green/brownish green in some samples to bright red/deep reddish brown in others. The majority of amphiboles are optically unzoned; some, however, show simple zoning with compositionally contrasting cores and rims (Fig. 2d). Many titanomagnetite microphenocrysts contain exsolution lamellae of ilmenite (Fig. 2e). The groundmass of the 1951 andesite is predominantly feldspathic with microlites of plagioclase, amphibole and Fe-Ti oxides. Xenocrystic olivine is present (e.g., Fig. 2f), typically with reaction coronae of amphibole ± orthopyroxene. Apatite, cristobalite

and zircon are accessory phases; apatite is found as inclusions in phenocrysts and cristobalite is mainly found inside vesicles.

Magmatic enclaves

Dark-coloured magmatic enclaves range from 12 mm to >50 mm based on hand specimen observations. They have sharp margins and no clear grain size variation within individual enclaves (Fig. 3a-d). Two major types of enclave are distinguished in hand specimen: those with a *diktytaxitic* texture and those with a *plutonic* texture.

Diktytaxitic textures in volcanic rocks are typified by a highly vesicular glassy groundmass and the presence of abundant elongated crystals (Bacon, 1986). In Mt. Lamington, diktytaxitic-textured enclaves (Fig. 3a) are characterized by the presence of glass, 3.7-16.3% sub-spherical vesicles or vesicle networks and abundant acicular amphibole crystals, with crystals protruding into the irregular-shaped vesicles. Phenocryst or antecryst phases in these enclaves consist of amphibole (40-47%), plagioclase (21-31%), Fe-Ti oxides (<3%), and biotite (<1%). Amphibole in the diktytaxitic enclaves occurs as: (i) large tabular crystals with compositionally distinct cores and rims (Fig. 4a,b), (ii) acicular crystals with long axes ranging from a few hundred microns to 2 mm (Fig. 4a,b), (iii) euhedral crystals growing as part of olivine reaction rims (Fig. 4a,b), (iv) amphibole xenocrysts rimmed by amphibole (Fig. 4e) and (v) in plutonic crystal clots with plagioclase and biotite, characterized by coarse, cumulus embayed crystals with minor amounts of glass present along grain boundaries (Fig. 4e,f). We term the tabular amphiboles *phenocryst-like* because the crystal morphology is similar to amphibole phenocrysts from the 1951 andesite (*antecrysts*). Plagioclase in the diktytaxitic enclaves occurs as square-shaped crystals (<0.5 mm), commonly with a resorbed core surrounded by normally zoned rim. Large plagioclase crystals with patchy and sieve textures are also found (e.g., Fig. 4d). Spinel-bearing olivine (1.3-4.3%) is present as an abundant relict phase with reaction rims of opx+oxides and amphibole (Fig. 2f, 4a-c).Olivine crystals tend to be euhedral when the reaction rim is thin (Fig. 4b). Rare clinopyroxenes are present and are characterized by breakdown textures such as amphibole rims and the development of amphibole blebs along their cleavage planes; thus they are identified as xenocrysts (Fig. 4a).

In contrast, the *plutonic-textured* enclaves (Fig. 3c,d) have lower vesicularity (4.9-8.0%), higher vesicle-free crystallinity (94.7-97.5%), and a larger grain size. They are composed of amphibole-dominated clusters (long axes up to 3-5 mm) with Fe-Ti oxide

inclusions, individual euhedral amphibole crystals (2-4 mm) and granular-poikilitic plagioclase (Fig. 5a,b). Amphibole is optically unzoned. Plagioclase is mainly normal or oscillatory zoned; some have spongy cores. Olivine is absent from these enclaves. The textural variation from diktytaxitic to plutonic appears to be gradational; this is evidenced by generally increasing crystallinity with decreasing glass and vesicle content (Fig. 3; 4b,c; Table 2). For convenience, those enclaves with intermediate texture (e.g., 13.8% vesicularity, 84.0% vesicle-free crystallinity, lacking olivine; Fig 3b) are grouped with the plutonic-textured enclave suite.

One of the plutonic-textured enclaves (sample LAM-10I, Fig. 3d) contains anomalously high proportions of amphibole compared with the other enclaves (69.1% compared with 40.3~48.0%, Table 2). The high amphibole content is consistent with the abundance of amphibole-dominated clusters (Fig. 3d, 6b). This enclave also contains a small region with distinctive coarse-grained texture that we speculate could represent part of a hornblendite nodule in this enclave (Fig. 3d). Some of the plagioclase from this enclave is poikilitic, filling the gaps between amphibole clusters, whereas others are granular with spongy cores and zoned interstitial overgrowths (Fig. 6a).

One plutonic-textured enclave contains abundant interstitial anhydrite, which is strongly altered, with a dark-coloured rim. Apatite is present as an accessory phase in all enclaves.

Pre-1951 shoshonite

The older lavas from the crater walls of Mt. Lamington are shoshonites (previously documented as *trachybasalt;* Arculus *et al.*, 1983). Compared to the 1951 andesite, the shoshonites are also porphyritic but contain far fewer phenocrysts/antecrysts, and are less vesicular. Phenocryst phases include subhedral olivine and Fe-Ti oxides, euhedral oscillatory-zoned plagioclase and extensively altered amphibole (Fig. 5c,d). The strongly resorbed, sieve-textured plagioclase is an antecryst phase (Fig. 5c). The groundmass consists of microcrystalline (150-200 μm) plagioclase, olivine, Fe-Ti oxides, orthopyroxene and clinopyroxene.

PUB xenoliths

A harzburgite and a dunite xenolith (Fig. 5e,f) hosted in the 1951 andesite have been interpreted as fragments of the PUB (Arculus *et al.*, 1983). An inner rim of orthopyroxene and outer rim of low-Al_2O_3 amphibole and/or phlogopite separate the xenoliths from the host andesite magma. Abundant chromite inclusions and numerous trails of fluid inclusions are present in the olivines which show cumulus embayed textures. The phenomena of kink-banding, wavy extinction and grain size reduction in the olivines are also evident. These are suggested to result from dislocation and granulation of larger primary crystals during solid-state deformation, as in previous studies (e.g., Jaques & Chappell, 1980).

Major and trace elements

Major element data (Arculus *et al.*, 1983) are reported in Table 1 and plotted in Fig. 7. The 1951 andesite and magmatic enclaves have bulk compositions of medium/high-K andesite (58.7-61.2 wt % SiO_2, 2.1-2.2 wt % K_2O) and medium-K basalt to basaltic andesite (49.0-54.2 wt % SiO_2, 1.1-1.7 wt % K_2O), respectively; the pre-1951crater wall-building lavas are shoshonitic (54.9-55.1 wt % SiO_2, 3.2-3.3 wt % K_2O; Le Maitre, 2002). The 1951 andesite suite has a narrow range of compositional variations, but linear arrays versus SiO_2 are seen for CaO, TiO_2, MgO and Na_2O+K_2O (Fig. 7a, c, d, f). The enclaves have a broader range of SiO_2 variation and CaO, TiO_2, MgO and FeO_{tot} progressively decrease with increasing SiO_2, whereas Na_2O+K_2O and Al_2O_3 increase. In plots of CaO, Na_2O+K_2O and TiO_2 versus SiO_2, the linear trends shown by the enclaves display a slight offset from the trends within the andesite suite (Fig. 7a, c, f).

Trace elements are plotted versus Rb in Fig. 8. The LILE (e.g. Ba, Sr) generally increase with Rb in the enclaves and andesite suite (Fig. 8a,b). Within individual suites of diktytaxitic and plutonic enclaves and the andesite, HFSE (e.g. Zr, Th and Nb) vary unsystematically with Rb (Fig. 8c-e). The REE (e.g., La, Ce and Dy) do not show clear variation trends with increasing Rb in the diktytaxitic and plutonic enclave suites, whereas in the 1951 andesite they display slightly negative trends (Fig. 8f). With increasing Rb, concentrations of compatible elements (e.g., Cr, Ni) in the 1951 andesite remain relatively unchanged at low levels; however, they decrease dramatically within the diktytaxitic and plutonic enclave suite (Fig. 8g,h).

Primitive mantle-normalized incompatible element patterns (Fig. 9a) show that the Mt. Lamington volcanic products have the typical trace element signature of subduction-related volcanism: depletions of HFSE (e.g. Zr, Nb, Th and U), together with enrichment of LILE (e.g. Rb, Sr) and LREE relative to middle (MREE) and heavy (HREE) rare earth elements (Tatsumi *et al.*, 1986; McCulloch & Gamble, 1991; Davidson, 1996; Pearce & Peate, 1995). The 1951 andesites are more enriched in LILE and depleted in MREE and HREE than the enclaves. The pre-1951 shoshonite has higher concentrations of the most incompatible trace elements compared to the 1951 andesite, but the two suites are indistinguishable in HREE and Pb. Chondrite-normalized REE patterns (Fig. 9b) are slightly concave, due to enrichment of LREE and a flat HREE profile. There is a slight negative Eu anomaly amongst all Mt. Lamington volcanic samples. The 1951 andesite REE patterns are slightly steeper than those of the enclaves. Within the enclave group, the plutonic enclaves are more enriched in MREE and HREE relative to the diktytaxitic enclaves. Unlike the light REE enriched pattern of the diktytaxitic enclaves, the REE pattern of the plutonic enclaves is S-shaped, with a peak at Pr.

Sr-Nd isotopes

Bulk rock Sr-Nd isotope data are shown in Fig. 10. The 1951 andesite and enclaves overlap isotopically. Both have small ranges in $^{87}Sr/^{86}Sr$ (0.7038-0.7040) and $^{143}Nd/^{144}Nd$ (0.51282-0.51290). The pre-1951 shoshonite is distinctive with lower $^{87}Sr/^{86}Sr$ (0.703683-0.703705). The harzburgite xenolith separated from the andesitic lava host has $^{87}Sr/^{86}Sr$ of 0.704096, higher than the Mt. Lamington volcanic samples, and $^{143}Nd/^{144}Nd$ of 0.512821. However, it is not clear how representative this is of the PUB; because of the very low Sr and Nd concentrations in the harzburgite, the isotopic composition is ultra-sensitive to surface weathering or sample contamination by the host andesite. All samples plot within the field of late Cenozoic volcanic rocks in southeast PNG (Fig. 10a; Hegner & Smith, 1992).

Mineral and glass chemistry

Amphibole

All amphiboles from the Mt. Lamington magmatic rocks are calcic ($[Ca]_{M4}$>1.5 atoms per formula unit (apfu)) with high $[Mg^{2+}/(Mg^{2+}+Fe^{2+})]_{M1-3}$ values of 0.68-0.99. They are classified as magnesiohornblende ($[Na+K]_A$<0.5, $[Si]_T$>6.5), tschermakite ($[Na+K]_A$<0.5, $[Si]_T$<6.5) and magnesiohastingsite ($[Na+K]_A$<0.5, $[Si]_T$<6.5, and $[Al]_{M1-3}$<$[Fe^{3+}]_{M1-3}$) following the classification of Leake *et al*. (1997) (Fig. 11a, Table 3).

Amphibole phenocrysts from the 1951 andesite display a large variation in SiO_2 (40.60-47.70 wt %), FeO_{tot} (8.33-17.22 wt %), MgO (11.81-17.22 wt %), and CaO (11.09-12.23 wt %) versus Al_2O_3 (7.46-13.35 wt %; Fig. 11b-d; Table 3). The Al-rich rims of zoned grains, and a small minority of other crystals, are also enriched in MgO and depleted in FeO, MnO and SiO_2.

Amphiboles rimming the PUB dunite xenolith have distinctively low Al_2O_3 (6.37-8.91 wt %), TiO_2 (0.82-1.27 wt %), Na_2O (1.59-1.96 wt %), and higher SiO_2 (47.24-48.46 wt %; Fig. 11f; Table 3).

In the diktytaxitic enclaves, phenocryst-like amphiboles have low-Al cores (8.39-10.80 wt % Al_2O_3), which are compositionally similar to amphibole phenocrysts from the 1951 andesite. The phenocryst-like amphiboles also have strongly zoned rims that are Al-rich in the inner rim (10.77-13.09 wt %) and less Al-rich in the outer rim (8.11-12.92 wt %). The Al-rich rims on these phenocryst-like grains are similar to the compositions of framework-forming (acicular) and olivine-rimming amphiboles in the diktytaxitic enclaves (10.59-13.22 wt % Al_2O_3; Table 3). They are also compositionally similar to the subset of Al-rich compositions observed within the andesite (Fig. 11).

In the plutonic-textured enclaves, amphiboles in crystal clusters have an Al_2O_3 range of 8.59-12.31 wt % (Table 3). They are similar in composition to amphibole phenocrysts from the andesite, but with slightly lower FeO_{tot} (12.31-15.58 wt %), and MnO (0.23-0.38 wt %), and slightly higher MgO (12.33-14.97 wt %; Fig. 11c-e; Table 3).

In the pre-1951 shoshonite the least-altered amphibole cores display limited compositional variation but are similar to the Al-rich amphiboles found in the diktytaxitic enclaves, albeit with higher TiO_2 , Na_2O and K_2O relative to those of the 1951 andesite (Fig. 11, Table 3).

Plagioclase

In the 1951 andesite, oscillatory zoned plagioclase phenocrysts frequently display a large compositional range (An_{30-60}; Arculus *et al.*, 1983). Patchy-zoned plagioclase is characterized by spongy cores (BSE-bright patch of $An_{41.7}$, dark patch of $An_{37.5}$) overgrown by oscillatory zoned rims ($An_{37.1-47.4}$). Sieve-textured plagioclases have anhedral oscillatory zoned cores (e.g. $An_{47.4}$) separated from a thin, more calcic, normally zoned rim (inner rim of $An_{60.5}$ and outer rim of $An_{39.1}$) by a layer of melt inclusions. Plagioclase microlites have the compositional range $An_{33.3-50.2}$ (Table 4).

In the diktytaxitic enclaves plagioclase is mainly normally zoned with a compositional range $An_{31.6-55.8}$. One large patchy-textured plagioclase has a BSE-bright patch of $An_{69.5}$, a dark patch of $An_{28.9}$ and a rim of $An_{42.9}$. In the plutonic-textured enclaves poikilitic plagioclase is either oscillatory ($An_{32.1-57.5}$) or patchy zoned (Table 4).

In the pre-1951 shoshonite, euhedral oscillatory-zoned plagioclase phenocrysts have an An range of 35.1-53.6, indistinguishable from those in the 1951 andesite and enclaves (Table 4).

Biotite-phlogopite

In the 1951 andesite biotite occurs as fresh euhedral phenocrysts (0.5-1.0 mm) and as inclusions in plagioclase and amphibole phenocrysts. These have homogeneous compositions (Mg-number 0.43-0.45, MnO 0.18-0.20 wt %, TiO_2 3.89-3.94 wt %, and F 0.26-0.29 wt %). In constrast, the reaction rim phase growing around the PUB harzburgite xenolith is phlogopite with a high Mg-number (0.51-0.65) and F content (0.42-0.69 wt %), and low MnO (0.09-0.12 wt %) and TiO_2 (0.19-2.76 wt %; Fig. 12, Table 5).

In the diktytaxitic enclaves biotite is not abundant (<2.4%), whereas in the plutonic-textured enclaves it is found as euhedral crystals in amphibole-dominated clusters, as inclusions in amphibole, or as interstitial grains. Their compositions are homogeneous and indistinguishable from those of biotite phenocrysts in the 1951 andesite (Mg-number 0.44~0.48, MnO 0.14~0.20, F 0.28~0.33; Fig. 12, Table 5).

Fe-Ti-Cr oxides

In the 1951 andesite, Fe-Ti oxides occur as microphenocrysts and microlites, and plagioclase- and amphibole-hosted mineral inclusions. The compositions of homogeneous (unexsolved) microphenocrysts range from low-Ti magnetite (4.61 wt % TiO_2, 0.16 wt % Cr_2O_3, 86.24 wt % FeO_{tot}) to titanomagnetite (22.72-32.26 wt% TiO_2, 0.04-0.05 wt % Cr_2O_3, 59.57-69.17 wt % FeO_{tot}; Fig. 13a,b, Table 6).

In the diktytaxitic enclaves, Fe-Ti-Cr oxides are present as microphenocrysts and mineral inclusions in olivine xenocrysts, as well in the reaction rims around olivine xenocrysts. Microphenocrysts are mainly low-Ti magnetite (4.41-8.81 wt % TiO_2; 76.96-84.38 wt % FeO_{tot}), with Cr_2O_3 contents (1.09-3.72 wt %) slightly higher than those in the 1951 andesite (Fig. 13a,b, Table 6). Inclusions in olivine xenocrysts and their reaction rims display a large range of variation in terms of Cr, Ti, Al and Mg-number (Fig. 13c-h; Table 6). Two chromian spinel inclusions found in unreacted olivine cores are characterized by high Cr (41.31-47.38 wt % Cr_2O_3), Al (13.87-14.08 wt % Al_2O_3) and low Ti (0.49-0.61 wt % TiO_2), in contrast to the Cr-bearing magnetite that occurs in the reaction rims of olivines (0.14-37.70 wt % Cr_2O_3, 1.50-9.30 wt % Al_2O_3, 0.35-8.69 wt % TiO_2; Fig. 13c, e-f; Table 6). In the plutonic-textured enclaves, Fe-Ti-Cr oxides are mainly present in amphibole-dominated clusters. They are Cr-bearing magnetite, with compositions similar to inclusions in olivine reaction rims in the diktytaxitic enclaves. They are distinguishable from magnetite microphenocrysts in the diktytaxitic enclaves by their higher Cr (5.90-12.90 wt %) and lower Ti (1.94-3.93 wt % TiO_2; Fig. 13a; Table 6). The chromite inclusions in the PUB xenoliths are strikingly different from the rest of the oxides found in the Mt Lamington magmatic rocks, with low Ti and high Cr (<0.06 wt % TiO_2; 53.96-59.50 wt % Cr_2O_3; Fig. 13a-h, Table 6).

In the pre-1951 shoshonite, one analysis of an oxide microphenocryst gives an ilmenite composition (31.87 wt % TiO_2, 0.08 wt % Cr_2O_3, 59.57 wt % FeO_{tot}; Table 6).

Olivine

Olivine xenocrysts containing Cr-spinel inclusions are present in both the andesite host lava and the diktytaxitic enclaves. Reaction rims have two parts; enstatite-rich orthopyroxene and minor Cr-bearing magnetite form the internal rim whereas the outer rim is dominated by amphibole (Fig. 2f). In olivines from the 1951 andesite the inner rim of opx+oxides is

commonly absent. Despite the reaction rim textures, some of the remnants of olivine preserve euhedral shapes (Fig. 4b), which are in striking contrast to the rounded, embayed texture of olivines from the PUB ultramafic xenoliths (e.g., Fig. 5e,f). Moreover, solid-state deformation textures such as kink-banding and granulation found in olivine from the PUB xenoliths are not observed. Compositions of olivine in the andesite magma are $Fo_{81.3} - Fo_{89.7}$, indistinguishable from those in the diktytaxitic enclaves (Table 7), suggesting a common source. In some relic olivines, there is a trend of decreasing forsterite content rimward within the crystal ($Fo_{88.2-81.2}$; Fig. 2f, Table 7).

These olivine xenocrysts are distinguishable from olivine in the PUB xenoliths, which have higher Fo contents ($Fo_{91.7-92.1}$) and NiO (0.34-0.42 wt %) but lower CaO (<0.02 wt %) and MnO (0.01-0.12 wt %; Fig. 14, Table 7). This is consistent with reported compositions for PUB harzburgite olivine ranging from $Fo_{91.6}$ to $Fo_{93.6}$ (England & Davies, 1973; Jaques & Chappell, 1980).

In the pre-1951 shoshonite, a single olivine microphenocryst has a composition of Fo_{85} and a trace element composition indistinguishable from olivine in the 1951 andesite and the diktytaxitic enclaves.

Pyroxenes

Pyroxenes are comparatively rare in the 1951 andesite, but both clinopyroxene and orthopyroxene are common as microphenocrysts or microlites in the pre-1951 shoshonite. The clinopyroxene microlites are diopside ($En_{44.5-45.6}$; Table 8). Pyroxenes in plutonic-textured enclaves are absent, whereas in diktytaxitic enclaves clinopyroxene is a rare xenocryst phase rimmed by amphibole ($En_{45.7-49.3}$; Fig. 4a), and orthopyroxene composes the inner rims of olivine xenocrysts ($En_{76.6-80.9}$; Fig. 2f, Table 8). Clinopyroxene xenocrysts in diktytaxitic enclaves are slightly more magnesian (high En content) and have higher Cr_2O_3 (0.21-0.66 wt %) and lower TiO_2 (0.26-0.49 wt %), Al_2O_3 (1.83-3.64 wt %), MnO (0.11-0.13 wt%) and Na_2O (0.25-0.33 wt %) than the microlites in the pre-1951 shoshonite (Table 8 and Supplementary Data Appendix Table). In the PUB harzburgite nodule, orthopyroxenes have a compositional range of En_{95-84}, (Arculus *et al.*, 1983); these are more magnesian than those composing the olivine reaction rims in the diktytaxitic enclaves.

Glass

Matrix glasses in the diktytaxitic enclaves are rhyolitic (73.29~77.76 wt % SiO_2), and are indistinguishable from the glasses in the plutonic enclaves (76.96-78.27 wt % SiO_2; Table 9). The groundmass of the 1951 andesite is full of microlites and thus not analysed.

DISCUSSION

Origin of olivine xenocrysts with Cr-spinel inclusions

Amphibole-dominated clusters represent fully reacted olivines

The olivine crystals in the diktytaxitic enclaves and the 1951 andesite are clearly in disequilibrium with the host melt, as demonstrated by reaction rims of opx+oxides and/or amphibole. This is consistent with observations at Mt. Pinatubo (Matthews *et al.*, 1992; Di Muro *et al.*, 2008), Lascar Volcano (Matthews *et al.*, 1994), Shiveluch Volcano (Dirksen *et al.*, 2006), Unzen Volcano (Browne *et al.*, 2006), and experimental reaction of forsteritic olivine with silicic melt (Coombs & Gardner, 2004). The decreasing Fo content towards the rims (e.g., $Fo_{88.2\text{-}81.2}$; Table 7, Fig. 2f), is interpreted to be a result of equilibration with the host andesite melt or melt trapped within the enclaves, by diffusion or reaction. This equilibration is also recorded by the spinel inclusions hosted in the olivines. Original chromian spinels away from the olivine reaction rims are characterized by high Mg-number, Fe^{2+}/Fe^{3+} ratio, Cr and Al content, and low Ti (Fig. 13b-h). The suite of Cr-spinels within or adjacent to reaction rims show a wide range of compositions, with a clear decrease in Cr and Al and corresponding enrichment in Fe^{3+} with decreasing Mg-number (Fig. 13e-g). In contrast, Fe-Ti oxide microphenocrysts in the diktytaxitic enclaves have much lower Cr-numbers, which are inherited from the melt.

The above distinction is important because it allows us to draw some infererences about the origin of the amphibole clusters in the plutonic-textured enclaves. Oxide inclusions in these clusters have Cr-numbers similar to the Cr-bearing magnetite in the olivine reaction rims from the diktytaxitic enclaves. This implies that their origins have affinity with Cr-spinel inclusions in olivine, and we therefore interpret the amphibole clusters with Fe-Ti oxide inclusions as derived from complete resorption of olivine, as observed at Arenal volcano (Reagan *et al.*, 1987). This is consistent with the gradual increase in olivine reaction rim

thickness with decreasing olivine modal abundance in the diktytaxitic enclaves. We suggest that the plutonic-textured enclaves represent the end-member of this process, with olivine completely reacted to form large amphibole clusters.

Olivines with Cr-spinel inclusions are not sourced from PUB

Arculus *et al.* (1983) suggested that the olivine crystals present in the Mt. Lamington 1951 andesite and enclaves have an ophiolitic (PUB) origin, supported by the presence of PUB fragments in Mt. Lamington andesite dome lavas. Thus the high Cr, Ni contents of the Lamington magmas were interpreted as a result of ophiolite contamination (Arculus *et al*. 1983). A similar interpretation has been given for the origins of olivine present in diktytaxitic enclaves from Mt. Pinatubo (Di Muro *et al.*, 2008). However in some Mt. Lamington diktytaxitic enclaves the euhedral shapes of olivine crystals are well preserved, despite the presence of reaction rims. This strongly suggests that the olivines have a magmatic origin and could not be sourced from PUB ultramafic rocks or gabbros in which the olivines are coarse grained, with rounded or embayed textures and trails of fluid inclusions (Jaques & Chappell, 1980), features also seen in the PUB nodules examined in this study. Moreover, the compositions of the olivine xenocrysts and their Cr-spinel inclusions are dissimilar to those from the PUB harzburgite and dunite (Figs. 13,14). We reject the hypothesis that the 1951 olivines originated from the PUB basalt, since according to Jaques & Chappell (1980) the PUB basalt is either aphanitic or rarely loaded with microphenocrysts of augite and plagioclase, which are not observed in the Mt. Lamington magmatic rocks. The distinctive mineral compositions of the 1951 olivines demonstrate that they are also not derived from the pre-1951 shoshonite magmas. Thus we rule out the possibility that the olivine crystals are derived from the PUB and believe they have some other magmatic origin. We will return to this question later.

Constraints on PUB contamination of Mt. Lamington magmas

We have demonstrated that the abundant olivine xenocrysts found in the Mt. Lamington magmas cannot be derived from the PUB. However, the presence of harzburgite and dunite nodules rimmed by phlogopite and amphibole is indisputable evidence of interaction with the PUB during andesite magma ascent towards the surface. This raises the question of how much

PUB contamination is feasible and to what extent the bulk-rock compositions might be affected by interaction with the PUB. This involves two factors: (1) incorporation of solid fragments that (presumably) can be picked out and thus, we assume, do not contribute to the bulk-rock composition; (2) partial melting of those solid fragments, which would easily contaminate the host melt, and thus the bulk-rock composition. The efficiency of melting and assimilation is controlled by factors such as the temperature of the magma, the compositional contrast between the magma and the PUB xenoliths (e.g., Mg-number of the melt and PUB olivine), the specific surface area of the PUB xenoliths, the degree of serpentinization of the PUB ultramafic xenoliths and the rigidity of the PUB xenoliths. In general, if PUB xenoliths without significant serpentinization were incorporated into a relatively cool, evolved magma, resorption would not be expected due to their highly refractory nature. If significant contamination did occur, the host melt should be geochemically fingerprinted with typical PUB signatures, such as high Cr and Ni concentrations and low incompatible element concentrations.

Arculus *et al.* (1983) reported that concentrations of Cr and Ni in the Mt. Lamington 1951 andesite are high compared with Bismarck volcanic arc literature data (Johnson, 1982). However, new ICP-MS trace element data from this study show that concentrations of Cr (64-141 ppm, with one exception of 252 ppm) and Ni (25-63 ppm) in the 1951 andesite are high, but do not significantly stand out from the large background dataset of the Bismarck Arc-New Britain Arc compositions, which includes hundreds of bulk-rock analyses of volcanic rocks (GEOROC, http://georoc.mpch-mainz.gwdg.de; Fig. 15). Instead, the enclaves have remarkably high Cr (284-1049 ppm) and Ni (57-286 ppm, with one exception of 1271 ppm). To evaluate whether this Cr and Ni could be provided by the Cr spinel-bearing olivine xenocrysts, we carried out a mass balance calculation using the observed NiO content of the olivines from the EPMA data (Table 7) and the observed modal abundance of olivine (Table 2). The andesite lavas and magmatic enclaves have average Ni concentrations of c.a. 40 and 150 ppm, respectively. To obtain the olivine- or PUB-free andesite and enclave magma compositions which have bulk Ni concentrations of ca. 20 and 50 ppm (putative values from the background dataset in Fig. 15), 0.8% and 4.1% of olivine with 2500 ppm Ni (according to EPMA data for Fo_{87-89} olivines) need to be subtracted, respectively. The point counting results show that the 1951 andesites contain up to 1.7% olivine, and the diktytaxitic enclaves contain 1.3-4.3% (vesicle-free; Table 2). The mass balance calculation results are in good agreement with point counting, which demonstrates that assimilating variable amounts of high Ni olivine

is enough to account for the bulk-rock Ni variations. Similarly, high bulk-rock Cr is attributed to the chromian spinel inclusions in those olivine xenocrysts. Thus we do not require extensive PUB assimilation in order to generate the observed bulk-rock compositions, as suggested by Arculus *et al*. (1983). We also note that assimilation of PUB fragments will be restricted by growth of narrow reaction rims of amphibole and, or phlogopite (Fig. 5e,f), which isolate the PUB components from the melt and prevent further reaction. In summary, we consider the effect of PUB contamination of the Mt. Lamington magmas to be insignificant.

Recycling of earlier-fractionated minerals

We have demonstrated that the Fo-rich olivines and their high Cr, Al spinel inclusions are not sourced from the PUB. Compositions of relict olivine cores, as well as chromian spinel inclusions, imply that they crystallized from a primitive melt (high Mg-number, high Cr and Ni contents). Amphibole crystals with rims of secondary amphibole, some attached to olivine relicts (Fig. 4c), are also clearly not derived from the enclave-forming magma or host andesite, on the basis of their textures. The same is true of the rare clinopyroxene xenocrysts with disequilibrium textures (Fig. 4a). These clinopyroxenes are slightly more magnesian and contain higher Cr and Ni, and lower Ti and Na than clinopyroxene microlites from the pre-1951 shoshonite (Table 8). This suggests that the clinopyroxene xenocrysts cannot be derived from the shoshonite lavas, consistent with our interpretations of the source of the Fo-rich olivines. We therefore suggest that these are all products of early-stage fractional crystallization of a more primitive melt that may be a precursor to the 1951 andesite or pre-1951 shoshonite magmas. We speculate that fractional crystallization may have taken place at high pressure where olivine and Cr-spinel are stable fractionating phases, giving rise to a crystal mush of olivine ± spinel ± amphibole ± clinopyroxene. The enclave-forming magma then remobilized and assimilated some of this crystal mush during ascent, prior to intruding into the 1951 andesite magma reservoir. This interpretation is consistent with recent studies of mafic volcanic rocks from SW Japan (Zellmer *et al*., 2014).

Small nodules of amph+plag+bi found in one of the diktytaxitic enclaves are characterized by the presence of glass along embayed grain boundaries (Fig. 4e,f). This phenomenon is similar to the textures observed in the plutonic enclaves (Fig.6b-d), and is also observed in cumulate nodules entrapped and erupted in lavas from elsewhere. These textures

have been interpreted to represent the primary melt-filled porosity in crystallising cumulates (Holness *et al.*, 2007). Therefore, the presence of these nodules in the diktytaxitic enclave seems to indicate recycling of earlier formed plutonic materials including amphibole and biotite.

Formation of the magmatic enclaves

The textures of the magmatic enclaves can yield information on the processes involved in their formation and thus the crystallisation conditions of the intruding mafic magma in the volcanic plumbing system. The diktytaxitic texture indicates rapid magma quenching and fast crystallization, which is typically produced when hot enclave magma is brought into direct contact with a large volume of relatively cool, more silicic magma and quenched to thermal equilibrium (Eichelberger, 1980; Bacon, 1986). Fast bubble nucleation due to second boiling in response to heat loss produces a low density foam layer, which enables the enclave magma to float upward into the overlying magma body and form inclusions (e.g., Eichelberger, 1980; Ban *et al.*, 2005; Browne *et al.*, 2006; Edmonds *et al.*, 2014).

The diktytaxitic texture is common and also found in magmatic enclaves from many other volcanoes, such as: Soufrière Hills, Montserrat (Murphy *et al.*, 2000; Edmonds *et al.*, 2014; Plail *et al.*, 2014); Narugo (Ban *et al.*, 2005) and Unzen (described as porphyritic; Browne *et al.*, 2006), Japan; Santorini, Greece (Martin *et al.*, 2006); Mt. Pinatubo, Philippines (Di Muro *et al.*, 2008). In most of these examples, plagioclase is the framework-forming phase, whereas in the enclaves from Mt. Lamington, as well as those from Mt. Pinatubo and some from Soufrière Hills, the framework is constructed by acicular amphibole crystals. The preferential crystallization of amphibole relative to plagioclase suggests crystallisation at high pressure and relatively high temperature (e.g., > 250 MPa, > 900 °C), and water-saturated conditions (e.g., Moore & Carmichael, 1998; Krawczynski *et al.*, 2012).

Compared with the diktytaxitic texture, the plutonic texture is consistent with a relatively prolonged cooling history. This is demonstrated by high vesicle-free crystallinity, and crystal clusters dominated by coarse, unzoned tabular amphiboles, which are believed to be derived from complete resorption of olivine crystals (see *Origin of olivine xenocrysts with Cr-spinel inclusions*). We interpret the plutonic-textured enclaves to have formed by slow crystallisation in the mushy margins of the enclave magma body. Floatation cannot be

triggered due to an insufficient bubble nucleation-driven density drop and increased viscosity (Bacon, 1986). Alternatively, the plutonic enclaves may be generated by forcible disruption of the crystal mush by a recharging magma (Sparks *et al.*, 1977; Pallister *et al.*, 1992; Nakamura, 1995).

The above interpretation is similar to the model proposed by Browne *et al.* (2006) to explain the juxtaposition of enclaves with textural variability in host magmas. According to this model the diktytaxitic enclaves can be produced as hybrid buoyant blobs at the mutual interface when hot enclave-forming magma intrudes below the host magma. Meanwhile, the rest of the intruding magma below the mutual interface experiences a relatively longer history of gradual crystallization at a slower rate of undercooling, resulting in a heavily crystalline margin. Subsequent recharge events may disrupt the margin and inject the fragments into the overlying magma, generating plutonic enclaves (Fig. 16).

Crystal transfer of 1951 andesite components to magmatic enclaves

We earlier described the large, simple zoned, tabular amphiboles from the diktytaxitic enclaves as *phenocryst-like* because they have a crystal morphology similar to the amphibole phenocrysts in the 1951 andesite. Moreover, the compositions of their cores are in agreement with the unzoned amphibole phenocrysts from the 1951 andesite host, and the rim compositions are consistent with the acicular and olivine-rimming amphibole crystals in the the diktytaxitic enclaves. This indicates that the rims of the phenocryst-like amphiboles, as well as the olivine-rimming amphiboles, must crystallize together with the acicular framework amphiboles during enclave magma quenching against the andesite. Therefore, the cores of the phenocryst-like amphiboles must be already present in the enclave magma prior to or during quenching. Given the close compositional similarity of these cores with the amphibole phenocrysts from the andesite, we propose that these phenocryst-like amphibole crystals are transferred from the andesite or andesite-related crystal mush to the enclave magma, during ascent, quenching and interaction of the enclave-forming magma with the andesite host. We infer that a similar process explains the presence of sieve-textured and patchy-zoned plagioclase in the enclaves, with crystal sizes equivalent to phenocrysts in the andesite host and much bigger than the microphenocrysts in the enclaves.

Crystal transfer from the andesite or andesite-related crystal mush to the enclave-forming magma must occur before the boundary between the two rheologically different magmas is rigid enough to become a barrier prohibiting crystal transfer from the andesite host during quenching (Ubide *et al.*, 2014). Assimilation of crystals could occur from a partially mobile crystal mush, or alternatively in the contact zone (foam layer) where the diktytaxitic enclaves are generated (Fig. 16a). This mechanical constraint is consistent with the plutonic-textured enclaves being relatively free from andesite components, as these are presumed to form in a more rigid part of the mush that does not significantly interact with the superjacent andesite (Fig. 16c).

We also observe evidence for return crystal transfer from the enclaves back into the andesite host. For example, amphibole phenocrysts with simple zoning must have been transferred into the enclave magma, where their Al-rich rims crystallised. However, they are now observed in the andesite magma. This may occur by disaggregation of magmatic enclaves during magma ascent or by shear within the chamber, as has been demonstrated at Soufrière Hills Volcano (Humphreys *et al.*, 2009). However, in the Mt. Lamington 1951 andesite, components that originated in the enclave-forming magma are rare and difficult to identify.

Trace element and isotope constraints on the petrogenesis of the Mt Lamington magmas

Source of the 1951 andesite and enclave-forming magma

The high LILE/HFSE and LILE/LREE ratios of the 1951 andesites and enclaves indicate enrichment of fluid-mobile elements in the magma source region, and are thus consistent with slab-derived input of fluids/melts into the mantle source region of these magmas. This supports previous work indicating that, although there is apparently no active subduction in the region, magma generation is primarily driven by subduction-related processes (Johnson *et al.*, 1978; Arculus *et al.*, 1983).

The overlapping Sr-Nd isotope compositions of the enclaves and the andesite indicate that the 1951 andesite and enclave-forming magma originated from a common source. This also rules out significant partial melting or assimilation of lower crustal material, as this is dominated by the Emo Metamorphics, with $^{143}Nd/^{144}Nd$ spanning a wide compositional range from 0.512744±13 to 0.513107±18 (Worthing & Crawford, 1996) that is distinct from the Mt.

Lamington compositions. To explore this further, we considered trace element ratios that do not vary significantly with crustal-level fractional crystallization, and may therefore indicate the source of the parental magmas, e.g., Zr/Nb (Elliott *et al.*, 1997). The 1951 andesites have Zr/Nb ratios in the range 27.7-34.3, while the enclaves overlap but display a larger Zr/Nb variation (15.0-33.3, Fig. 17). Zr/Nb is insensitive to fractional crystallisation of olivine, pyroxenes and plagioclase, but amphibole can fractionate Zr from Nb as a result of differences in ionic charge and site preferences, with the relative partition coefficients for Zr and Nb depending on the composition of both amphibole and melt (Tiepolo *et al.*, 2001). Ba/La ratios of amphiboles from Mt. Pinatubo, Mt. St. Helens and Mt. Hood eruption products vary from approximately 2-8 for magnesiohornblende and 6-28 for tschermakite, whereas Zr/Nb ratios typically range from 5-20 (Fig. 17; Loewen, 2013). Therefore, fractionation or incorporation of amphibole, particularly of magnesiohornblende or tschermakite composition, could in principle significantly affect the trace element ratios of the bulk-rocks. We suggest that the differences in Zr/Nb and Ba/La between the enclave and andesite rock suites can be explained either by more extensive fractional crystallisation of hornblende from the andesites, pushing their trace element ratios to higher values, and/or by incorporation of foreign amphibole crystals, including earlier fractionated cumulate amphibole, by the enclaves, dragging their trace element ratios to lower values. This process could also explain the variations of trace element concentrations with Rb (Fig. 8), which is strongly depleted in amphibole but enriched in biotite.

Formation of the 1951 andesite and enclave-forming magma

Formation of intermediate magmas is typically ascribed to either shallow fractional crystallisation of mantle-derived mafic magmas, deep fractionation of wet mantle-derived mafic magmas, dehydration melting of amphibolitic lower crust, or mixing between mafic and felsic magmas, as summarised by Annen *et al*. (2006). The lack of isotopic heterogeneity among the andesites and enclaves, and their dissimilarity to the Emo Metamorphics precludes the possibility that significant dehydration partial melting of amphibolitic lower crust gave rise to the Mt. Lamington andesites. Therefore, to understand the formation of the 1951 andesite we must consider fractional crystallisation and mixing processes.

While there is clear evidence of bimodal magmatism and mixing, and some degree of hybridisation between the mafic enclaves and the andesite clearly does occur, incorporation

and hybridisation of enclave material into the andesite is not considered to have a significant effect on bulk-rock compositions, based on petrology and offsets in geochemical trends. Hence, fractional crystallization is required to explain the geochemistry of the 1951 andesite.

The 1951 andesite has low MgO and low Cr and Ni concentrations, which suggests that previous fractionation of ferromagnesian mineral phases, such as olivine, pyroxenes, Fe-Ti oxides and amphibole, has taken place from the parental melt. There is no significant Eu anomaly in the chondrite-normalised REE patterns (Fig. 12b), indicating that plagioclase is not a major phase in the fractionating assemblage. Lack of fractionation between the MREE and HREE suggests amphibole rather than garnet is involved in the fractionation assemblage. We suggest that the xenocrysts of ol+sp ± cpx ± amph observed in the diktytaxitic enclaves may represent remnants of this earlier phase of fractionation. This is consistent with recent experimental studies showing that deep crystallisation of hydrous basalt produces ol + cpx + amph + plag (Melekhova *et al.*, 2015), as well as the presence of cumulate nodules in Lesser Antilles lavas that contain these phases (Arculus & Wills, 1980). Thus we conclude that at Mt. Lamington, mafic cumulates are produced in the lower crust and sampled by the replenishing enclave-forming magma (Fig. 16).

The andesites themselves show limited geochemical variations and thus provide little direct evidence of an earlier differentiation history. However, extensions to the linear trend lines in plots of major elements versus SiO_2 intersect the tie-lines between the amphibole and plagioclase compositional groups (Fig. 7). Thus the compositional variations of the andesites are consistent with fractionation of a mineral assemblage involving amphibole and plagioclase (amphibole > plagioclase). We suggest that this represents a second stage of shallow-level fractional crystallisation (Fig. 16).

On the other hand, the magmatic enclaves are hybrids of foreign components and original melt in various proportions, having assimilated olivine. This explains the unsystematic variations within the diktyatxitic and plutonic enclaves in trace element plots (Fig. 8) and the S-shaped REE patterns of the plutonic enclaves (Fig. 9b), which cannot be reproduced by numerical modelling assuming that the enclaves represent magmatic liquids. It also explains why the observed modal assemblages of the plutonic-textured enclaves (dominated by amphibole + plagioclase) do not match what is expected for a magma of basaltic bulk composition.

CONCLUSIONS

Two major types of mafic-intermediate magmatic enclaves are identified within the andesitic dome lavas produced during the 1951eruption of Mt. Lamington: diktytaxitic and plutonic-textured. Diktytaxitic enclaves are formed when the enclave magma is quenched against the overlying andesite magma and generates a foam layer, which floats upward into the andesite magma. In contrast, the plutonic-textured enclaves represent slow-cooling crystallization products of the enclave-forming magma away from the direct contact zone with the andesite magma.

Both andesite and enclaves contain abundant olivine crystals with amphibole reaction rims, which appear to be responsible for the high Cr and Ni concentrations in the Mt. Lamington magmas. Contamination of the magmas by the PUB is not necessary and would seem to require an unreasonable thermal budget. The olivines are euhedral and do not show deformation textures, as observed in the PUB olivines; additionally their geochemical signatures are inconsistent with the PUB harzburgite and dunite xenoliths. Therefore the olivines cannot have an ophiolite origin, and instead are suggested to be products of earlier fractional crystallization from magmas that may have been precursor(s) to the 1951 andesite and/or pre-1951 shoshonite. Their presence, as well as that of xenocrysts of clinopyroxene and amphibole, are probably a result of remobilization and recycling by the enclave-forming magma.

Evidence for crystal exchange between the enclaves and the andesite host is seen in the petrology and further confirmed with mineral data. Isotopic data constrain the 1951 andesite and enclave-forming magma to have the same magma source; trace element signatures indicate a subduction-related component. We interpret variable trace element ratios to be a result of significant fractionation or assimilation of amphibole. The dominant processes that led to forming the 1951 andesite and enclave-bearing magma are likely to be deep fractional crystallization of mafic phases followed by shallow fractionation of amphibole ± plagioclase.

ACKNOWLEDGEMENTS

We thank Richard Arculus for providing the samples and background information. Ian Chaplin and Chris Ottley are thanked for their help during sample preparation and ICP-MS

analysis, Leon Bowen and Chris Hayward for help in SEM imaging and EPMA. Yaoling Niu, Helen Williams and members of the Durham Volcanology research group are thanked for constructive discussions. Reviews by Brandon Browne and two anonymous reviewers are gratefully acknowledged.

FUNDING

This work forms part of the first author's PhD research, which is funded by a Durham University doctoral scholarship and the China Scholarship Council. MCSH was supported by a Royal Society University Research Fellowship.

REFERENCES

Arculus, R. J., Johnson, R. W., Chappell, B. W., Mc Kee, C. O. & Sakai, H. (1983). Ophiolite-contaminated andesites, trachybasalts, and cognate inclusions of Mount Lamington, Papua New Guinea: anhydrite-amphibole-bearing lavas and the 1951 cumulodome. *Journal of Volcanology and Geothermal Research* 18, 215-247.

Arculus, R. J. & Wills, K. J. A. (1980). The Petrology of Plutonic Blocks and Inclusions from the Lesser Antilles Island Arc. *Journal of Petrology* 21, 743-799.

Bacon, C. R. (1986). Magmatic inclusions in silicic and intermediate volcanic rocks. *Journal of Geophysical Research* 91, 6091-6112.

Baldwin, S. L., Fitzgerald, P. G. & Webb, L. E. (2012). Tectonics of the New Guinea Region. *Annual Review of Earth and Planetary Sciences* 40, 495-520.

Ban, M., Takahashi, K., Horie, T. & Toya, N. (2005). Petrogenesis of Mafic Inclusions in Rhyolitic Lavas from Narugo Volcano, Northeastern Japan. *Journal of Petrology* 46, 1543-1563.

Browne, B. L., Eichelberger, J. C., Patino, L. C., Vogel, T. A., Dehn, J., Uto, K. & Hoshizumi, H. (2006). Generation of porphyritic and equigranular mafic enclaves during magma recharge events at Unzen volcano, Japan. *Journal of Petrology* 47, 301-328.

Coombs, M. L. & Gardner, J. E. (2004). Reaction rim growth on olivine in silicic melts: Implications for magma mixing. *American Mineralogist* 89, 748-758.

Davidson, J. P. (1996). Deciphering mantle and crustal signatures in subduction zone magmatism. In: Bebout, G. E., Scholl, D. W., Kirby, S. H. & Platt, J. P. (eds.) *Subduction Top to Bottom*. Washington, D. C.: American Geophysical Union, 251-262.

Davidson, J. P., Boghossian, N. D. & Wilson, M. (1993). The Geochemistry of the Igneous Rock Suite of St Martin, Northern Lesser Antilles. *Journal of Petrology* 34, 839-866.

Davies, H. L. (2012). The geology of New Guinea - the cordilleran margin of the Australian continent. *Episodes* 35, 87-102.

Davies, H. L. & Jaques, A. L. (1984). Emplacement of ophiolite in Papua New Guinea. *Geological Society, London, Special Publications* 13, 341-349.

Davies, H. L. & Smith, I. E. (1971). Geology of Eastern Papua. *Geological Society of America Bulletin* 82, 3299-3312.

Di Muro, A., Pallister, J., Villemant, B., Newhall, C., Semet, M., Martinez, M. & Mariet, C. (2008). Pre-1991 sulfur transfer between mafic injections and dacite magma in the Mt. Pinatubo reservoir. *Journal of Volcanology and Geothermal Research* 175, 517-540.

Dirksen, O., Humphreys, M. C. S., Pletchov, P., Melnik, O., Demyanchuk, Y., Sparks, R. S. J. & Mahony, S. (2006). The 2001-2004 dome-forming eruption of Shiveluch volcano, Kamchatka: Observation, petrological investigation and numerical modelling. *Journal of Volcanology and Geothermal Research* 155, 201-226.

Dosso, L., Bougault, H., Beuzart, P., Calvez, J. Y. & Joron, J. L. (1988). The Geochemical Structure of the Southeast Indian Ridge. *Earth and Planetary Science Letters* 88, 47-59.

Edmonds, M., Humphreys, M. C. S., Hauri, E. H., Herd, R. A., Wadge, G., Rawson, H., Ledden, R., Plail, M., Barclay, J., Aiuppa, A., Christopher, T. E., Giudice, G. & Guida, R. (2014). Pre-eruptive vapour and its role in controlling eruption style and longevity at Soufriere Hills Volcano. *Geological Society, London, Memoirs* 39, 291-315.

Eichelberger, J. C. (1980). Vesiculation of Mafic Magma during Replenishment of Silicic Magma Reservoirs. *Nature* 288, 446-450.

Elliott, T., Plank, T., Zindler, A., White, W. & Bourdon, B. (1997). Element transport from slab to volcanic front at the Mariana arc. *Journal of Geophysical Research* 102, 14991-15019.

England, R. N. & Davies, H. L. (1973). Mineralogy of Ultramafic Cumulates and Tectonites from Eastern-Papua. *Earth and Planetary Science Letters* 17, 416-425.

Hall, R. & Spakman, W. (2002). Subducted slabs beneath the eastern Indonesia-Tonga region: insights from tomography. *Earth and Planetary Science Letters* 201, 321-336.

Hegner, E. & Smith, I. E. (1992). Isotopic compositions of late Cenozoic volcanics from southeast Papua New Guinea-- Evidence for multi-component sources in arc and rift environments. *Chemical Geology* 97, 233-249.

Hill, K. C. & Raza, A. (1999). Arc-continent collision in Papua Guinea: Constraints from fission track thermochronology. *Tectonics* 18, 950-966.

Holness, M. B., Anderson, A. T., Martin, V. M., Maclennan, J., Passmore, E. & Schwindinger, K. (2007). Textures in Partially Solidified Crystalline Nodules: a Window into the Pore Structure of Slowly Cooled Mafic Intrusions. *Journal of Petrology* 48, 1243-1264.

Humphreys, M. C. S., Christopher, T. & Hards, V. (2009). Microlite transfer by disaggregation of mafic inclusions following magma mixing at SoufriSre Hills volcano, Montserrat. *Contributions to Mineralogy and Petrology* 157, 609-624.

Ito, E., White, W. M. & Gopel, C. (1987). The O, Sr, Nd and Pb Isotope Geochemistry of Morb. *Chemical Geology* 62, 157-176.

Jakeš, P. & Smith, I. E. (1970). High potassium calc-alkaline rocks from Cape Nelson, Eastern Papua. *Contributions to Mineralogy and Petrology* 28, 259-271.

Jaques, A. L. & Chappell, B. W. (1980). Petrology and trace element geochemistry of the Papuan Ultramafic belt. *Contributions to Mineralogy and Petrology* 75, 55-70.

Johnson, R. W. (1982). Papua New Guinea. In: Thorpe, R. S. (ed.) *Andesites*. London: John Wiley & Sons, 225-244.

Johnson, R. W., Mackenzie, D. E. & Smith, I. E. (1978). Delayed partial melting of subduction-modified mantle in Papua New Guinea. *Tectonophysics* 46, 197-216.

Krawczynski, M. J., Grove, T. L. & Behrens, H. (2012). Amphibole stability in primitive arc magmas: effects of temperature, H2O content, and oxygen fugacity. *Contributions to Mineralogy and Petrology* 164, 317-339.

Le Maitre, R. W. (2002). *Igneous rocks: A Classification and Glossary of Terms*: Cambridge University Press, Blackwell.

Leake, B. E., Woolley, A. R., Arps, C. E. S., Birch, W. D., Gilbert, M. C., Grice, J. D., Hawthorne, F. C., Kato, A., Kisch, H. J., Krivovichev, V. G., Linthout, K., Laird, J., Mandarino, J. A., Maresch, W. V., Nickel, E. H., Rock, N. M. S., Schumacher, J. C., Smith, D. C., Stephenson, N. C. N., Ungaretti, L., Whittaker, E. J. W. & Guo, Y. Z. (1997). Nomenclature of amphiboles: Report of the subcommittee on amphiboles of the International Mineralogical Association, Commission on New Minerals and Mineral Names. *Canadian Mineralogist* 35, 219-246.

Loewen, M. W. (2013). Volatile mobility of trace metals in volcanic systems. PhD thesis, Oregon State University, 177-200.

Lus, W. Y., McDougall, I. & Davies, H. L. (2004). Age of the metamorphic sole of the Papuan Ultramafic Belt ophiolite, Papua New Guinea. *Tectonophysics* 392, 85-101.

Mahoney, J. J., Natland, J. H., White, W. M., Poreda, R., Bloomer, S. H., Fisher, R. L. & Baxter, A. N. (1989). Isotopic and Geochemical Provinces of the Western Indian-Ocean Spreading Centers. *Journal of Geophysical Research-Solid Earth and Planets* 94, 4033-4052.

Martin, V. M., Holness, M. B. & Pyle, D. M. (2006). Textural analysis of magmatic enclaves from the Kameni Islands, Santorini, Greece. *Journal of Volcanology and Geothermal Research* 154, 89-102.

Matthews, S. J., Jones, A. P. & Bristow, C. S. (1992). A Simple Magma-Mixing Model for Sulfur Behavior in Calc-Alkaline Volcanic-Rocks - Mineralogical Evidence from Mount-Pinatubo 1991 Eruption. *Journal of the Geological Society* 149, 863-866.

Matthews, S. J., Jones, A. P. & Gardeweg, M. C. (1994). Lascar Volcano, Northern Chile - Evidence for Steady-State Disequilibrium. *Journal of Petrology* 35, 401-432.

McCulloch, M. T. & Gamble, J. A. (1991). Geochemical and geodynamical constraints on subduction zone magmatism. *Earth and Planetary Science Letters* 102, 358-374.

Melekhova, E., Blundy, J., Robertson, R. & Humphreys, M. (2015). Experimental evidence for polybaric differentiation of primitive arc basalt beneath St. Vincent, Lesser Antilles. *Journal of Petrology* 56, 161-192.

Michard, A., Montigny, R. & Schlich, R. (1986). Geochemistry of the Mantle beneath the Rodriguez Triple Junction and the Southeast Indian Ridge. *Earth and Planetary Science Letters* 78, 104-114.

Moore, G. & Carmichael, I. S. E. (1998). The hydrous phase equilibria (to 3 kbar) of an andesite and basaltic andesite from western Mexico: constraints on water content and conditions of phenocryst growth. *Contributions to Mineralogy and Petrology* 130, 304-319.

Murphy, M. D., Sparks, R. S. J., Barclay, J., Carroll, M. R. & Brewer, T. S. (2000). Remobilization of andesite magma by intrusion of mafic magma at the Soufriere Hills Volcano, Montserrat, West Indies. *Journal of Petrology* 41, 21-42.

Nakamura, M. (1995). Continuous Mixing of Crystal Mush and Replenished Magma in the Ongoing Unzen Eruption. *Geology* 23, 807-810.

Ottley, C. J., Pearson, D. G. & Irvine, G. J. (2003). A routine method for the dissolution of geological samples for the analysis of REE and trace elements via ICP-MS. In: Holland, J. G. & Tanner, S. D. (eds.) *Plasma Source Mass Spectrometry: Applications and Emerging Technologies*. Cambridge: Royal Society of Chemistry, 221-230.

Pallister, J. S., Hoblitt, R. P. & Reyes, A. G. (1992). A Basalt Trigger for the 1991 Eruptions of Pinatubo Volcano. *Nature* 356, 426-428.

Pearce, J. A. & Peate, D. W. (1995). Tectonic Implications of the Composition of Volcanic Arc Magmas. *Annual Review of Earth and Planetary Sciences* 23, 251-285.

Plail, M., Barclay, J., Humphreys, M. C. S., Edmonds, M., Herd, R. A. & Christopher, T. E. (2014). Characterization of mafic enclaves in the erupted products of Soufriere Hills Volcano, Montserrat, 2009 to 2010. *Geological Society, London, Memoirs* 39, 343-360.

Reagan, M. K., Gill, J. B., Malavassi, E. & Garcia, M. O. (1987). Changes in magma compostion at Arenal volcano, Costa Rica, 1968–1985: real-time monitoring of open-system differentiation. *Bulletin of Volcanology* 49, 415-434.

Richard, P., Shimizu, N. & Allegre, C. J. (1976). $^{143}Nd/^{146}Nd$, a natural tracer: an application to oceanic basalts. *Earth and Planetary Science Letters* 31, 269-278.

Smith, I. E. (1982). Volcanic evolution in eastern Papua. *Tectonophysics* 87, 315-333.

Smith, I. E. & Milsom, J. S. (1984). Late Cenozoic volcanism and extension in Eastern Papua. *Geological Society, London, Special Publications* 16, 163-171.

Smith, I. E. M. (2013a). High-magnesium andesites: the example of the Papuan Volcanic Arc. *Geological Society, London, Special Publications* 385, 117-135.

Smith, I. E. M. (2013b). The chemical characterization and tectonic significance of ophiolite terrains in southeastern Papua New Guinea. *Tectonics* 32, 159-170.

Smith, I. E. M. & Compston, W. (1982). Strontium Isotopes in Cenozoic Volcanic-Rocks from Southeastern Papua-New-Guinea. *Lithos* 15, 199-206.

Smith, I. E. M., Taylor, S. R. & Johnson, R. W. (1979). REE-fractionated trachytes and dacites from Papua New Guinea and their relationship to andesite petrogenesis. *Contributions to Mineralogy and Petrology* 69, 227-233.

Sparks, S. R. J., Sigurdsson, H. & Wilson, L. (1977). Magma mixing: a mechanism for triggering acid explosive eruptions. *Nature* 267, 315-318.

Staudigel, H., McCulloch, M. T., Zindler, A. & Perfit, M. R. (1987). Complex ridge subduction and island arc magmatism: an isotopic study of the New Georgia Forearc

and the Woodlark Basin. In: Taylor, B. & Exon, N. F. (eds.). Houston, TX, United States (USA): Circum-Pacific Council for Energy and Mineral Resources, 227-240.

Sun, S. S. & McDonough, W. F. (1989). Chemical and isotopic systematics of oceanic basalts: implications for mantle composition and processes. *Geological Society, London, Special Publications* 42, 313-345.

Tatsumi, Y., Hamilton, D. L. & Nesbitt, R. W. (1986). Chemical characteristics of fluid phase released from a subducted lithosphere and origin of arc magmas: Evidence from high-pressure experiments and natural rocks. *Journal of Volcanology and Geothermal Research* 29, 293-309.

Taylor, B., Goodliffe, A., Martinez, F. & Hey, R. (1995). Continental Rifting and Initial Sea-Floor Spreading in the Woodlark Basin. *Nature* 374, 534-537.

Taylor, B., Goodliffe, A. M. & Martinez, F. (1999). How continents break up: insights from Papua New Guinea. *Journal of Geophysical Research* 104, 7497-7512.

Taylor, G. A. (1958). The 1951 eruption of Mount Lamington, Papua. *Bureau of Mineral Resources, Geology and Geophysics* 38.

Tiepolo, M., Bottazzi, P., Foley, S. F., Oberti, R., Vannucci, R. & Zanetti, A. (2001). Fractionation of Nb and Ta from Zr and Hf at mantle depths: the role of titanian pargasite and kaersutite. *Journal of Petrology* 42, 221-232.

Ubide, T., Gale, C., Larrea, P., Arranz, E., Lago, M. & Tierz, P. (2014). The Relevance of Crystal Transfer to Magma Mixing: a Case Study in Composite Dykes from the Central Pyrenees. *Journal of Petrology* 55, 1535-1559.

van der Plas, L. & Tobi, A. C. (1965). A chart for judging the reliability of point counting results. American Journal of Science 263, 87-90.

Wallace, L. M., Stevens, C., Silver, E., McCaffrey, R., Loratung, W., Hasiata, S., Stanaway, R., Curley, R., Rosa, R. & Taugaloidi, J. (2004). GPS and seismological constraints on active tectonics and arc-continent collision in Papua New Guinea: Implications for mechanics of microplate rotations. *Journal of Geophysical Research-Solid Earth* 109, B05404.

Weissel, J. K., Taylor, B. & Karner, G. D. (1982). The Opening of the Woodlark Basin, Subduction of the Woodlark Spreading System, and the Evolution of Northern Melanesia since Mid-Pliocene Time. *Tectonophysics* 87, 253-277.

Worthing, M. A. & Crawford, A. J. (1996). The igneous geochemistry and tectonic setting of metabasites from the Emo Metamorphics, Papua New Guinea; A record of the evolution and destruction of a backarc basin. *Mineralogy and Petrology* 58, 79-100.

Zellmer, G. F., Sakamoto, N., Iizuka, Y., Miyoshi, M., Tamura, Y., Hsieh, H. H. & Yurimoto, H. (2014). Crystal uptake into aphyric arc melts: insights from two-pyroxene pseudo-decompression paths, plagioclase hygrometry, and measurement of hydrogen in olivines from mafic volcanics of SW Japan. Orogenic Andesites and Crustal Growth 385, 161-184.

FIGURE CAPTIONS

Fig. 1. (a) Regional map of the Papuan Peninsula, surrounding basins, subduction zones (both active and inactive) and seafloor spreading centres (after Baldwin *et al.*, 2012; Davies, 2012); (b) simplified geological map of the Papuan Peninsula (after Davies, 2012; Smith, 2013a), indicating the position of Mt. Lamington and three other major volcanic edifices, the Papuan Ultramafic Belt (PUB), Owen Stanley Metamorphic Complex, Milne Terrane and Aure Fold Belt.

Fig. 2. Backscattered SEM images illustrating the mineralogical and textural features of the 1951 andesite (a-e) and diktytaxitic enclave (f): (a) oscillatory zoned plagioclase phenocryst; (b) patchy-zoned plagioclase; (c) sieve-textured plagioclase; (d) simple-zoned amphibole phenocryst; (e) an ilmenite-magnetite pair, the magnetite crystal contains exsolution lamellae of ilmenite; (f) an olivine xenocryst from a diktytaxitic enclave, showing a reaction rim of opx+ Fe-Ti oxides and amphibole, and inclusions of chromian spinel. The greyscale variation within the olivine relict corresponds to the compositional variation: the darker core and brighter rim represent $Fo_{88.2}$ and $Fo_{81.2}$, respectively. *plag* – plagioclase; *amph* – amphibole; *mgt* – magnetite; *ilm* – ilmenite; *ol* – olivine; *Cr sp* – chromian spinel.

Fig. 3. Magmatic enclaves hosted in the 1951 andesite displaying textural variations. (a) diktytaxitic enclave LAM-8; (b) enclave intermediate between diktytaxitic texture and plutonic texture, LAM-25; (c) plutonic enclave (LAM-6I); (d) plutonic enclave with up to 69% amphibole (LAM-10I); this also contains an amphibole-rich region with a distinctive coarse-grained texture. See text for details.

Fig. 4. Photomicrographs illustrating the mineralogical features of the diktytaxitic enclaves: (a) xenocrysts of clinopyroxene and olivine; (b) euhedral olivine xenocryst and acicular and phenocryst-like amphiboles; (c) amphibole xenocryst attached to olivine reaction relics, rimmed by secondary amphibole; (d) andesite-derived patchy-zoned plagioclase, with grain size contrasting to crystals from the diktytaxitic enclaves; (e,f) an amph-plag-bi nodule found in a diktytaxitic enclave; amphibole crystals are cumulus with an embayed texture, with minor glass present along the grain boundaries (indicated by white arrows).

Fig. 5. Photomicrographs of plutonic enclave (a,b), pre-1951 shoshonite (c,d) and PUB xenoliths hosted in the 1951andesite (e,f). (a) Overgrowth of granular plagioclase with progressive crystallization; (b) Anhedral plagioclase in contact with melt (glass) in an

anhydrite-bearing plutonic enclave (LAM-17I); (c) altered amphibole and sieve-textured plagioclase phenocrysts in a microcrystalline groundmass; (d) altered amphibole and olivine microphenocrysts, and orthopyroxene and plagioclase microlites; (e,f) dunite and harzburgite xenoliths from the PUB incorporated in the 1951 andesite; the xenoliths are rimmed by orthopyroxene and amphibole ± phlogopite.

Fig. 6. Backscattered SEM images showing the textural features of the plutonic enclaves: (a) a spongy-cored plagioclase grain with zoned interstitial overgrowth; (b-d) amphibole-biotite clusters composed of subhedral-anhedral crystals and melt (glass) entrapped by the overgrowth of crystal grains. These features demonstrate the process of formation of a crystalline mush which has been observed in cumulates previously (e.g., Holness *et al.*, 2007).

Fig. 7. Major element variation diagrams for Mt. Lamington volcanic samples; data from Arculus *et al*. (1983). Analytical uncertainties are overlapped by the symbol sizes. Grey fields labelled as *amph* and *plag* represent amphibole and plagioclase compositions determined by EPMA; stars represent the average composition of amphibole and plagioclase; solid lines demonstrate the variation trends of enclaves and andesites; extrapolation of the trend lines of the andesites intersect the dashed line, linking average compositions of amphibole and plagioclase, suggesting that fractional crystallization of amphibole and plagioclase gives rise to the 1951 andesite compositional variations. See text for details.

Fig. 8. Trace element (ppm) variation diagrams for the Mt. Lamington volcanic samples. Representative analytical uncertainties of ICP-MS data are shown by the error bars on each plot; analytical uncertainties for Zr (XRF; Arculus *et al.*, 1983) are unknown.

Fig. 9. (a) Primitive mantle normalized incompatible trace element patterns and (b) Chondrite normalized REE patterns for the 1951 andesite, magmatic enclaves and pre-1951 shoshonite. Normalization values from Sun & McDonough (1989).

Fig. 10. (a,b) Sr-Nd isotopic compositions of the Mt. Lamington 1951 andesites, pre-1951 shoshonites, diktytaxitic enclaves, plutonic enclaves and the PUB harzburgite xenolith; (b) is an enlargement of the data shown in (a). Shown for comparison are fields for Pacific MORB, Woodlark Basin and Southeast Indian Ridge MORB: data from Michard *et a*l. (1986), Ito *et al*. (1987), Staudigel *et al*. (1987), Dosso *et al*. (1988) and Mahoney *et al*. (1989). Also shown is a field for Late Cenozoic rocks from southeast PNG (including rift volcanics, arc volcanics and high-K trachytes, data from Hegner & Smith, 1992).

Fig. 11. (a) Amphibole compositions plotted in the classification diagram of Leake *et al.* (1997); $[Na+K]_A$ and $[Si]_T$ are calculated according to the amphibole stoichiometry procedure of Leake *et al.* (1997); (b-f) Chemical variations (wt %) of amphiboles from Mt. Lamington volcanic samples; representative 1 σ analytical uncertainties are illustrated as error bars.

Fig. 12. Variation of TiO_2 versus MnO (a) and F versus Mg-number (b) for biotite from the 1951 andesite and plutonic enclaves. These have contrasting compositions to the phlogopite rimming the PUB harzburgite. Mg-number = $Mg/(Mg+Fe^{2+})$; representative 1 σ errors are indicated.

Fig. 13. Compositional variations of Fe-Ti-Cr oxides from Mt. Lamington volcanic samples and PUB xenoliths. Molecular percentages of Fe^{3+}, Cr and Al are calculated according to the spinel stoichiometry; Mg-number = $Mg/(Mg+Fe^{2+})$. Analytical uncertainties are overlapped by the symbol sizes. See text for details.

Fig. 14. Compositional variations of olivines from the Mt. Lamington volcanic samples and PUB xenoliths; representative 1 σ errors are given in the plots. See text for details. (a) MnO, (b) NiO and (c) CaO versus forsterite mol%.

Fig. 15. Ni (ppm) variations versus SiO_2 (wt %) for the 1951 andesite, pre-1951 shoshonite and the magmatic enclaves. Grey pluses are comparison data for the Bismarck Arc-New Britain Arc (GEOROC, http://georoc.mpch-mainz.gwdg.de). The arrows on the enclaves and andesite indicate the effect of subtracting the observed amount of olivine (from vesicle-free modal analysis, Table 2), and point towards the inferred original composition before olivine assimilation. Magmatic enclaves with Ni > 200 ppm (LAM-9I, -19I and 20I) are not shown on this plot due to unavailable major element data of those samples (see Table 1).

Fig. 16. Schematic cartoons of the Mt. Lamington magma system: (a) the compositional evolution of 1951 andesite is represented by shallow fractional crystallization of amphibole+plagioclase; the interrelationship between the magmatic enclaves and the andesite host is represented by enclave-forming magma intrusion into the andesite magma; earlier-fractionated crystals recycle through the recharging magma percolating crystal mushes; (b,c) the formation of diktytaxitic and plutonic-textured enclaves; (d) recycling of earlier-fractionated olivines from an old crystal mush through enclave-forming magma percolation; (b) and (c) are after Browne *et al.* (2006). See text for details.

Fig. 17. Zr/Nb versus Ba/La for the 1951 andesite, pre-1951 shoshonite and the magmatic enclaves. The shaded fields illustrate the range of Zr/Nb and Ba/La ratios in amphiboles from Mt. Pinatubo, Mt. Hood and Mt. St. Helens (Lowen, 2013), which have compositions of magnesiohornblende (mg-hbl), tschermakite (tsch) and magnesiohastingsite (mg-hst). The difference in Zr/Nb and Ba/La ratios between the magmatic enclaves and the 1951 andesite can be explained either by more extensive fractional crystallisation of amphibole from the andesites, pushing their trace element ratios to higher values, or by recycling foreign amphibole crystals, including earlier fractionated cumulate amphibole, by the enclaves, reducing their trace element ratios to lower values.

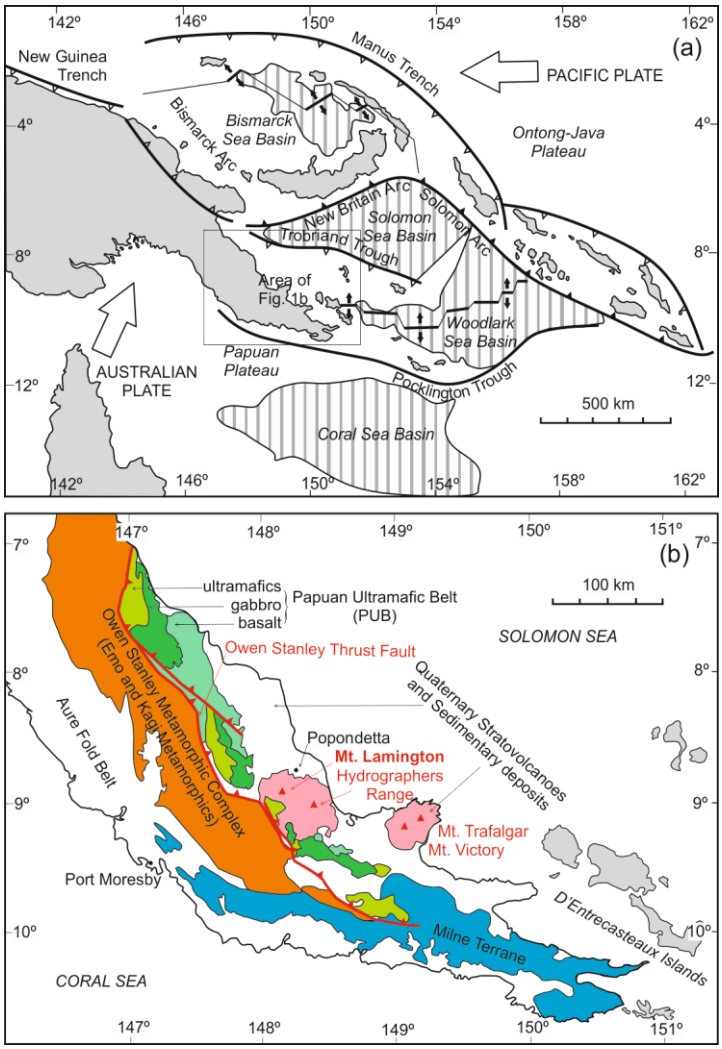
(a)
New Guinea Trench
Manus Trench
PACIFIC PLATE
Bismarck Arc
Bismarck Sea Basin
Ontong-Java Plateau
New Britain Arc
Solomon Sea Basin
Solomon Arc
Trobriand Trough
Area of Fig. 1b
Woodlark Sea Basin
Papuan Plateau
AUSTRALIAN PLATE
Pocklington Trough
500 km
Coral Sea Basin
(b)
100 km
ultramafics
gabbro
basalt
Papuan Ultramafic Belt (PUB)
SOLOMON SEA
Owen Stanley Thrust Fault
Owen Stanley Metamorphic Complex (Emo and Kagi Metamorphics)
Quaternary Stratovolcanoes and Sedimentary deposits
Aure Fold Belt
Popondetta
Mt. Lamington
Hydrographers Range
Mt. Trafalgar
Mt. Victory
Port Moresby
D'Entrecasteaux Islands
Milne Terrane
CORAL SEA

Fig. 1

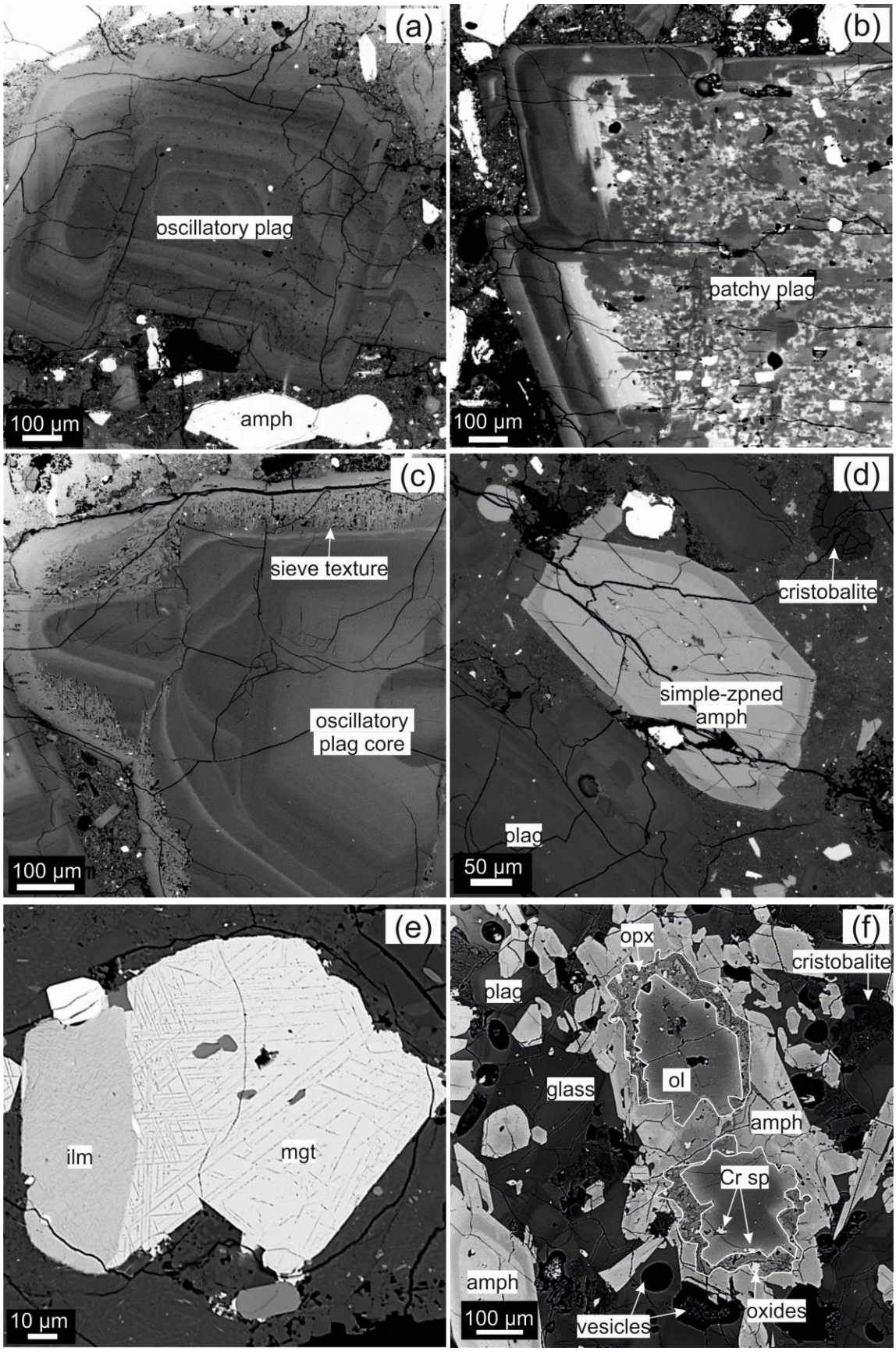
(a)
oscillatory plag
amph
100 µm
(b)
patchy plag
100 µm
(c)
sieve texture
oscillatory
plag core
100 µm
(d)
cristobalite
simple-zpned
amph
plag
50 µm
(e)
ilm
mgt
10 µm
(f)
opx
cristobalite
plag
glass
ol
amph
Cr sp
amph
100 µm
vesicles
oxides

Fig. 2

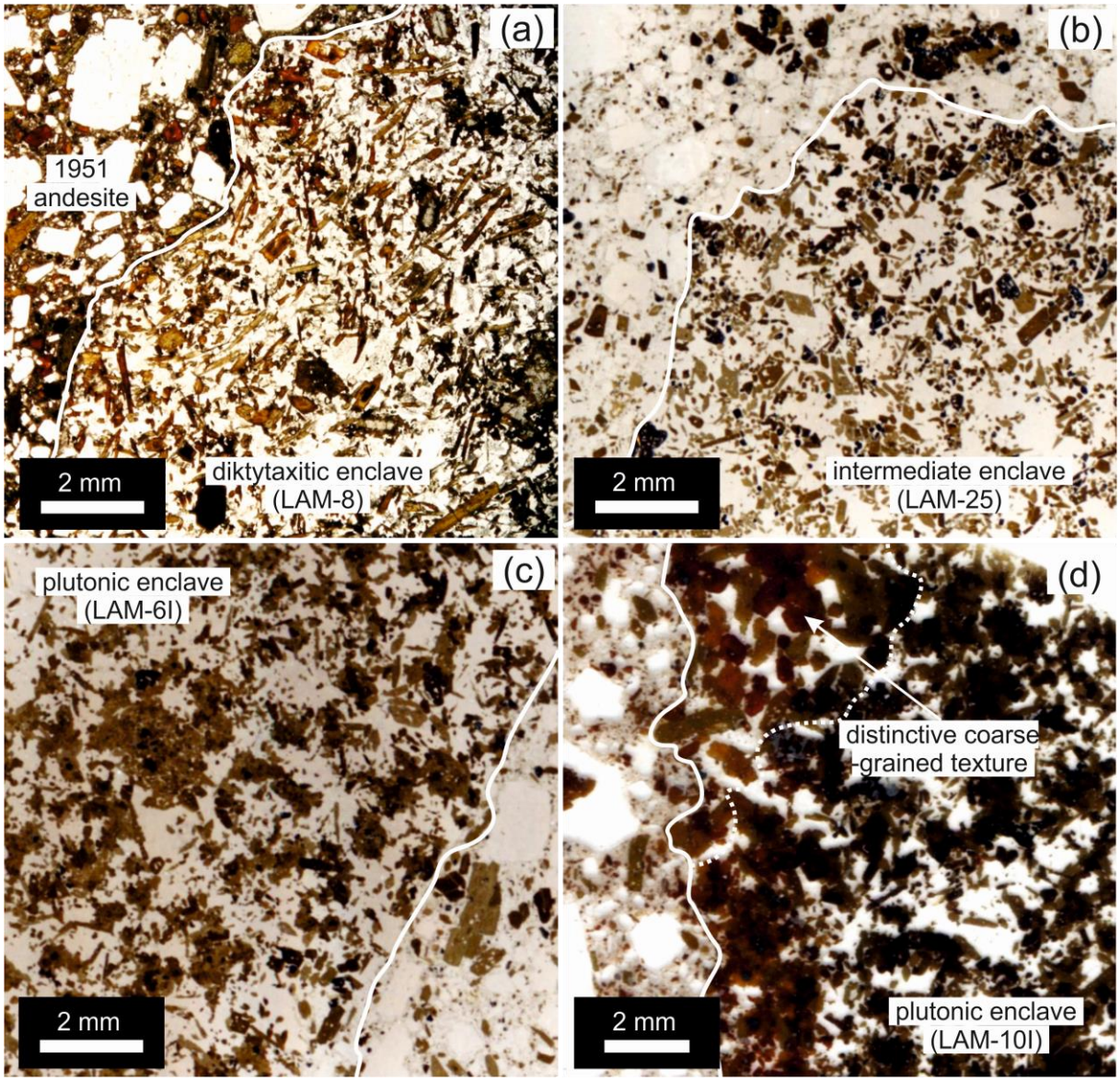
(a)
1951
andesite
2 mm
diktytaxitic enclave
(LAM-8)
(b)
2 mm
intermediate enclave
(LAM-25)
plutonic enclave
(LAM-6I)
(c)
2 mm
(d)
distinctive coarse
-grained texture
2 mm
plutonic enclave
(LAM-10I)

Fig. 3

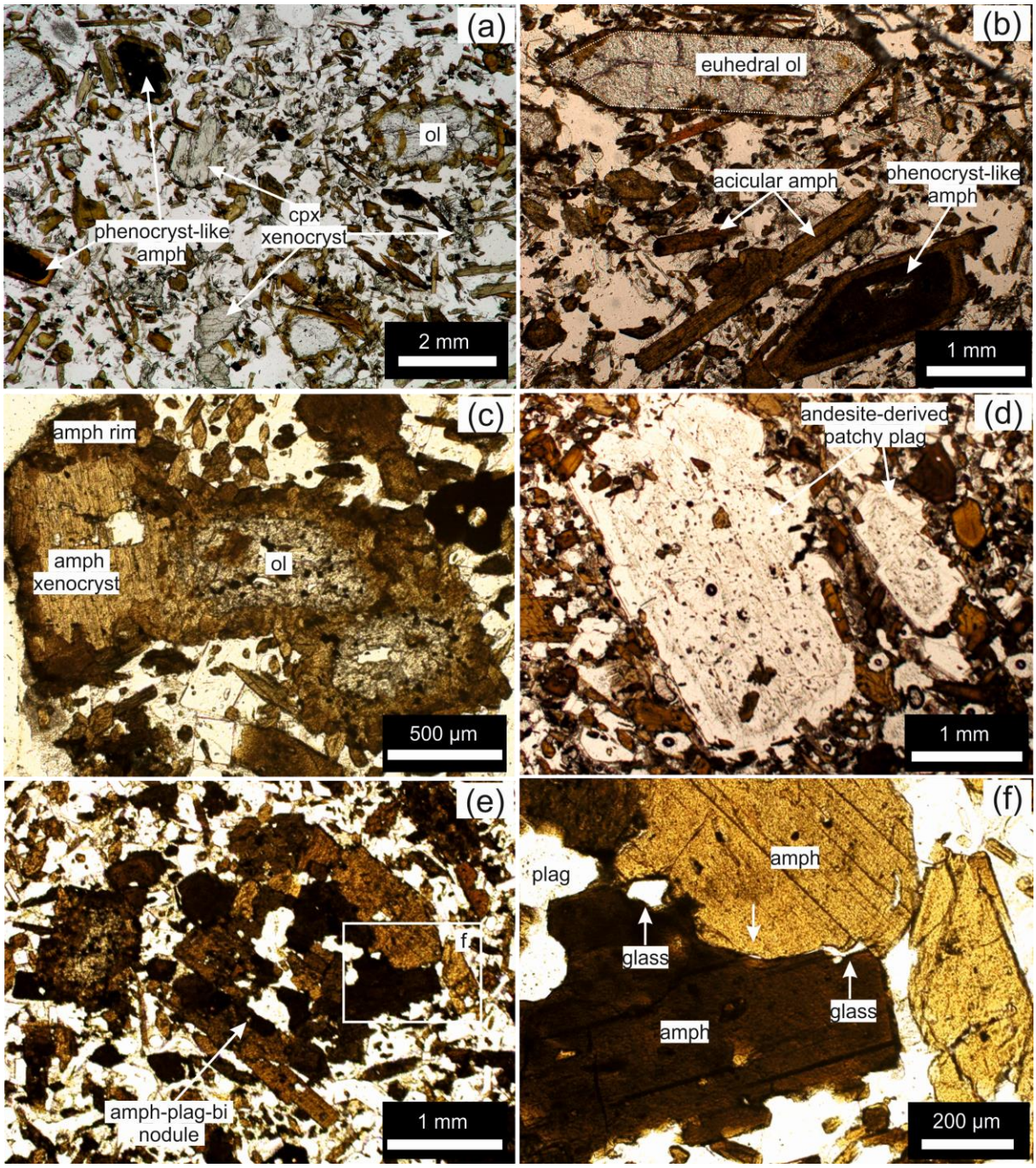
(a)
ol
phenocryst-like amph
cpx xenocryst
2 mm
(b)
euhedral ol
acicular amph
phenocryst-like amph
1 mm
(c)
amph rim
amph xenocryst
ol
500 µm
(d)
andesite-derived patchy plag
1 mm
(e)
f
amph-plag-bi nodule
1 mm
(f)
plag
amph
glass
glass
amph
200 µm

Fig. 4

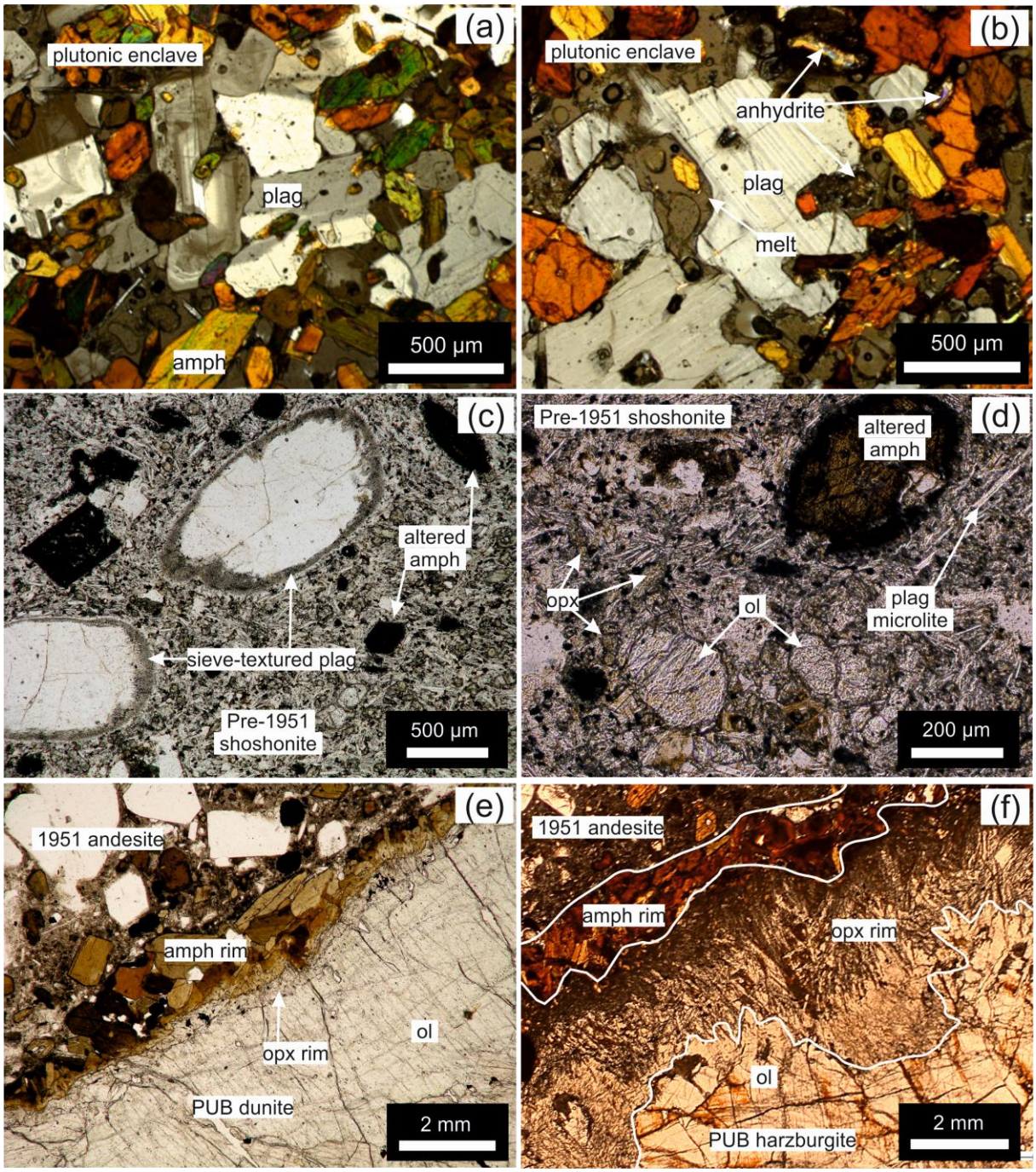
(a)
plutonic enclave
plag
amph
500 µm
(b)
plutonic enclave
anhydrite
plag
melt
500 µm
(c)
altered amph
sieve-textured plag
Pre-1951 shoshonite
500 µm
(d)
Pre-1951 shoshonite
altered amph
opx
ol
plag microlite
200 µm
(e)
1951 andesite
amph rim
opx rim
ol
PUB dunite
2 mm
(f)
1951 andesite
amph rim
opx rim
ol
PUB harzburgite
2 mm

Fig. 5

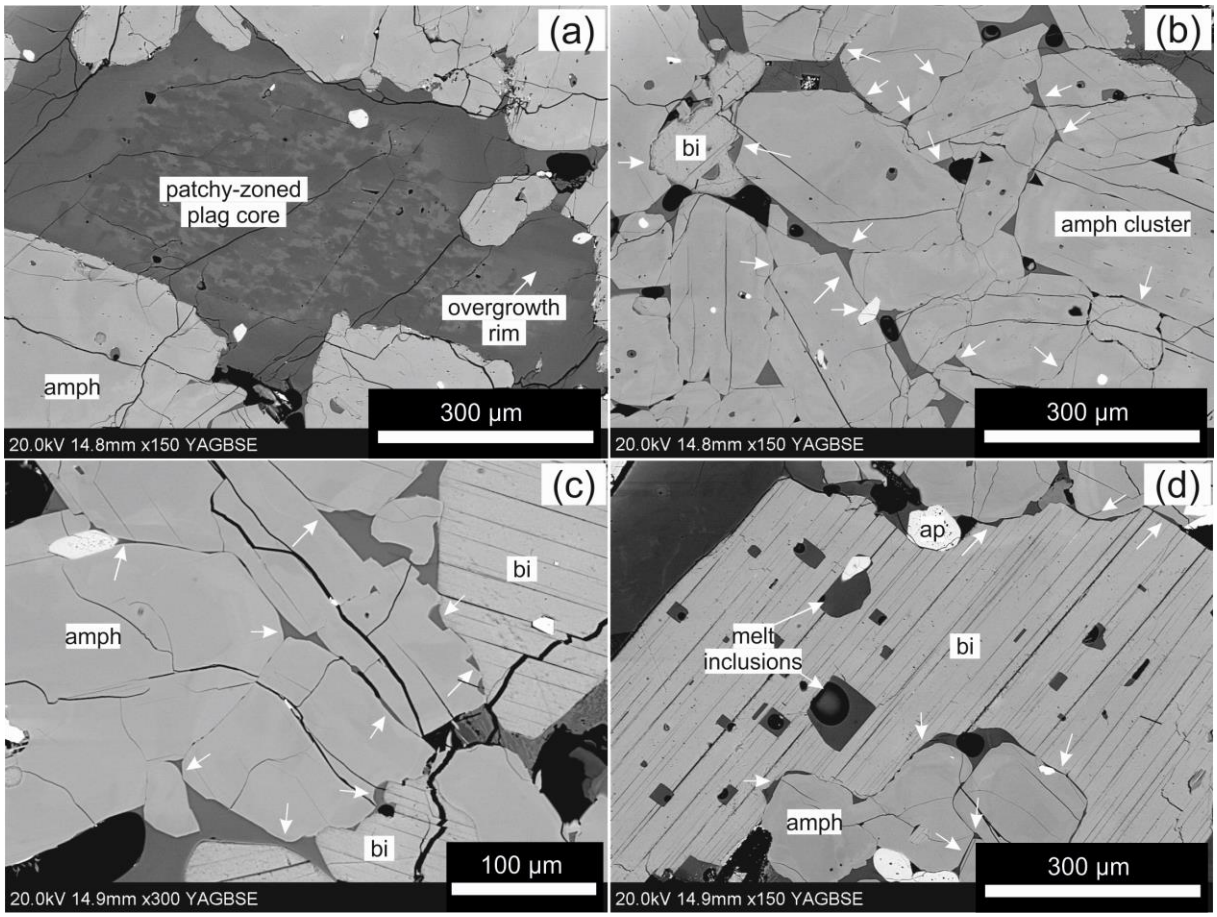
(a)
patchy-zoned
plag core
overgrowth
rim
amph
300 µm
20.0kV 14.8mm x150 YAGBSE
(b)
bi
amph cluster
300 µm
20.0kV 14.8mm x150 YAGBSE
(c)
bi
amph
bi
100 µm
20.0kV 14.9mm x300 YAGBSE
(d)
ap
melt
inclusions
bi
amph
300 µm
20.0kV 14.9mm x150 YAGBSE

Fig. 6

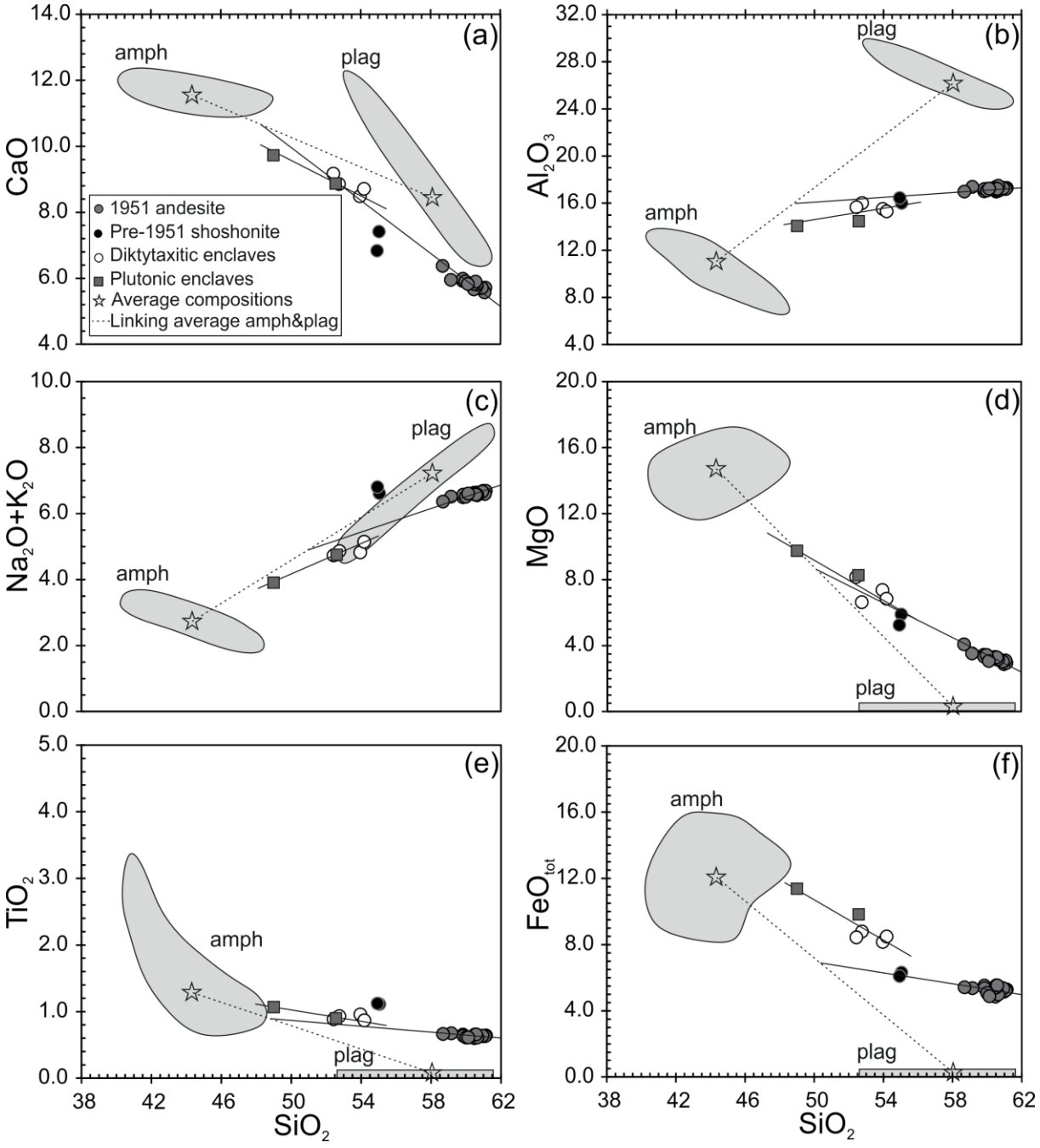
(a)
(b)
(c)
(d)
(e)
(f)
amph
plag
1951 andesite
Pre-1951 shoshonite
Diktytaxitic enclaves
Plutonic enclaves
Average compositions
Linking average amph&plag
CaO
Al2O3
Na2O+K2O
MgO
TiO2
FeOtot
SiO2

Fig. 7

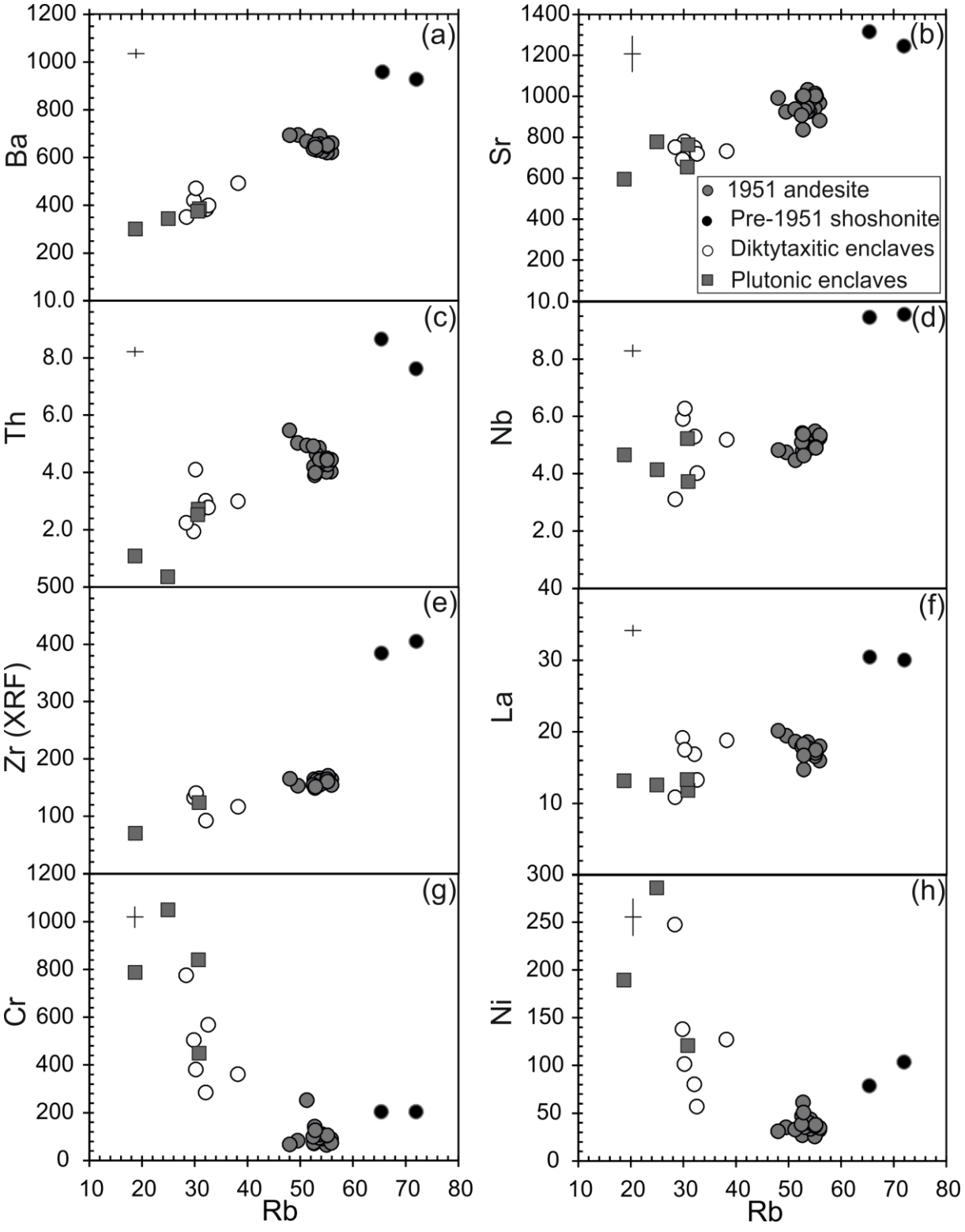
(a)
Ba
(b)
Sr
1951 andesite
Pre-1951 shoshonite
Diktytaxitic enclaves
Plutonic enclaves
(c)
Th
(d)
Nb
(e)
Zr (XRF)
(f)
La
(g)
Cr
(h)
Ni
Rb
Rb

Fig. 8

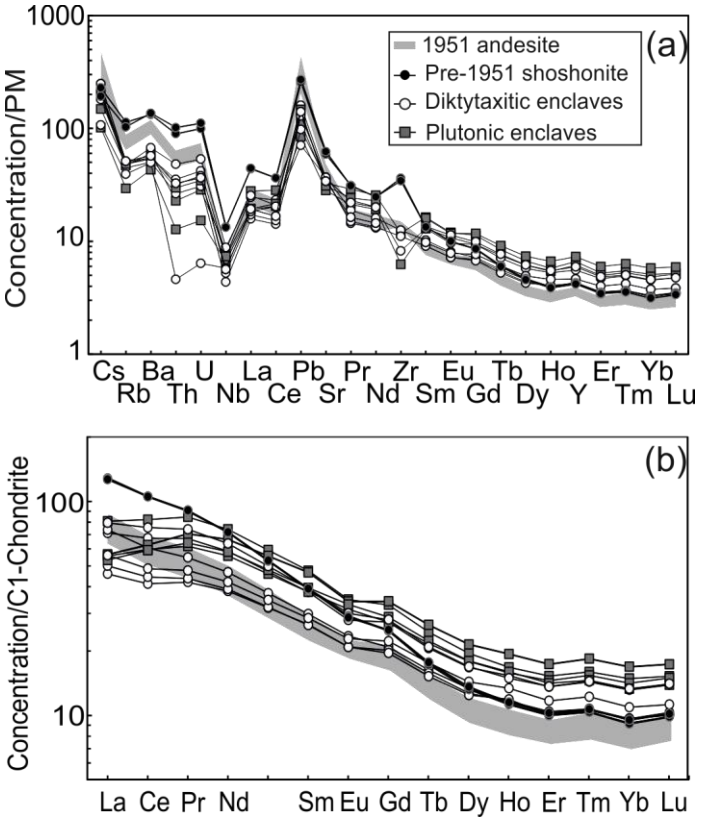
1000
100
10
1
Concentration/PM
1951 andesite
Pre-1951 shoshonite
Diktytaxitic enclaves
Plutonic enclaves
(a)
Cs Rb Ba Th U Nb La Ce Pb Sr Pr Nd Zr Sm Eu Gd Tb Dy Ho Y Er Tm Yb Lu
(b)
100
10
Concentration/C1-Chondrite
La Ce Pr Nd Sm Eu Gd Tb Dy Ho Er Tm Yb Lu

Fig. 9

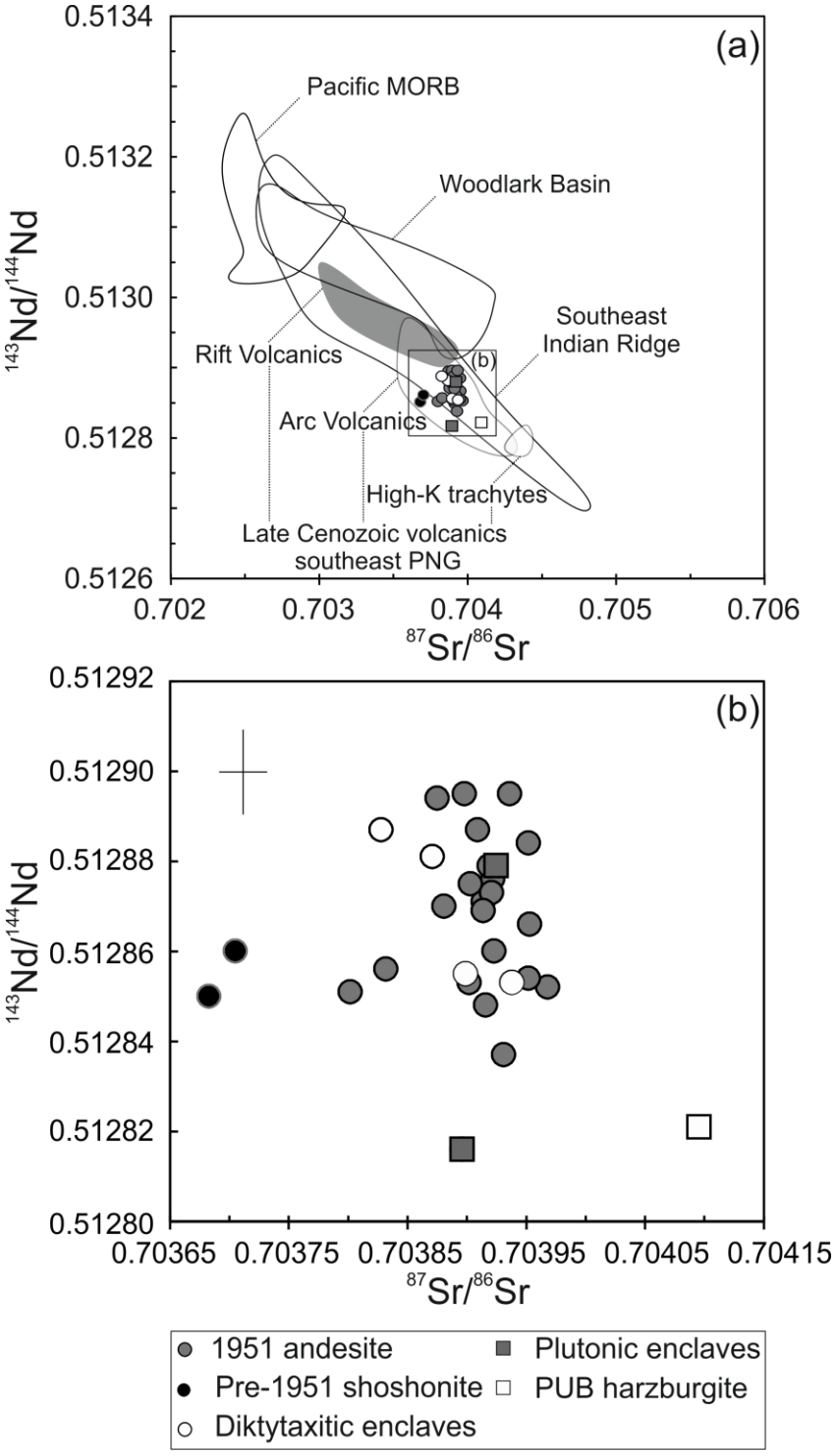
(a)
Pacific MORB
Woodlark Basin
Southeast
Indian Ridge
Rift Volcanics
(b)
Arc Volcanics
High-K trachytes
Late Cenozoic volcanics
southeast PNG
0.5134
0.5132
0.5130
0.5128
0.5126
0.702
0.703
0.704
0.705
0.706
143Nd/144Nd
87Sr/86Sr
(b)
0.51292
0.51290
0.51288
0.51286
0.51284
0.51282
0.51280
0.70365
0.70375
0.70385
0.70395
0.70405
0.70415
143Nd/144Nd
87Sr/86Sr
1951 andesite
Pre-1951 shoshonite
Diktytaxitic enclaves
Plutonic enclaves
PUB harzburgite

Fig. 10

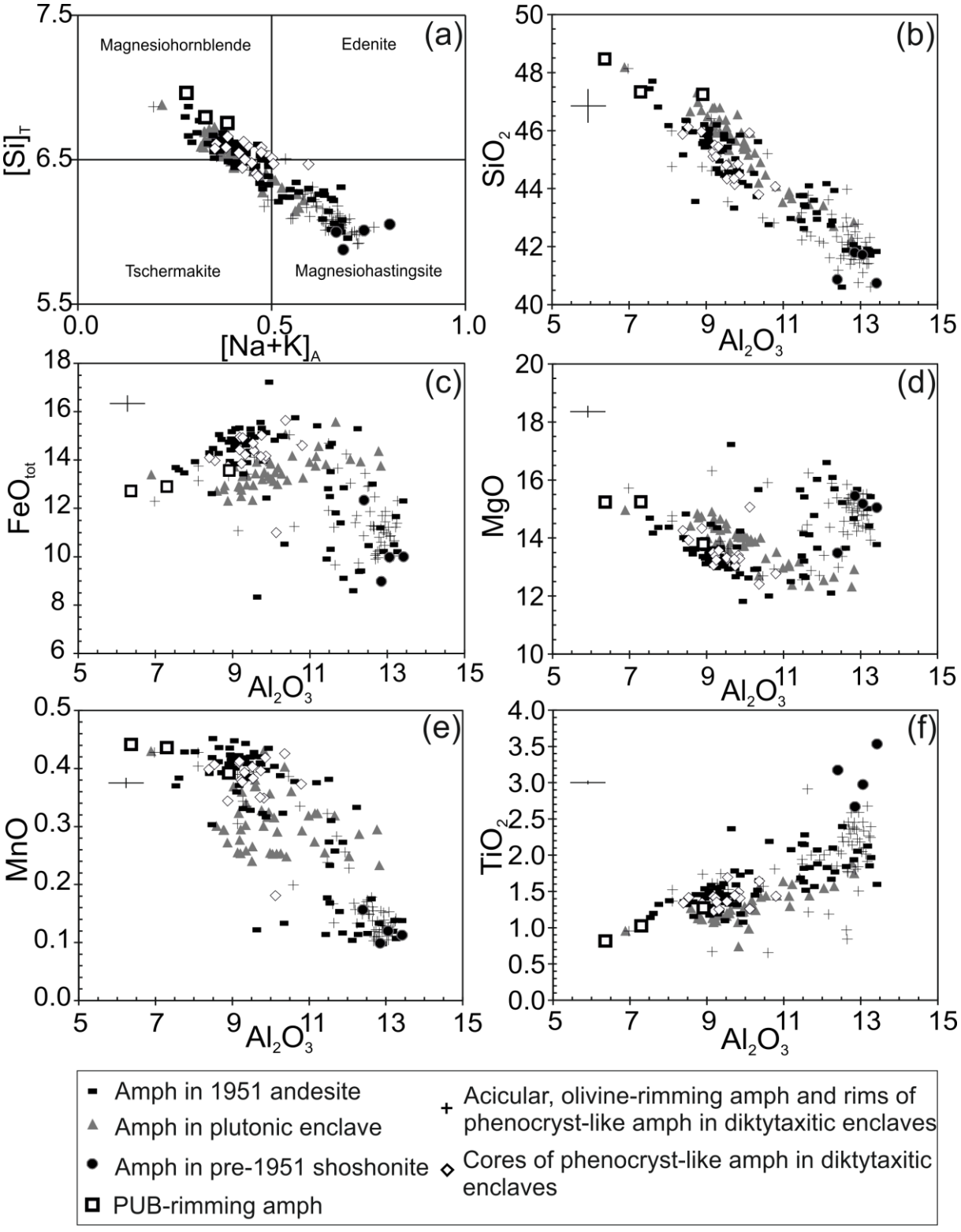
(a)
Magnesiohornblende
Edenite
Tschermakite
Magnesiohastingsite
[Si]T
[Na+K]A
(b)
SiO2
Al2O3
(c)
FeOtot
Al2O3
(d)
MgO
Al2O3
(e)
MnO
Al2O3
(f)
TiO2
Al2O3
Amph in 1951 andesite
Amph in plutonic enclave
Amph in pre-1951 shoshonite
PUB-rimming amph
Acicular, olivine-rimming amph and rims of phenocryst-like amph in diktytaxitic enclaves
Cores of phenocryst-like amph in diktytaxitic enclaves

Fig. 11

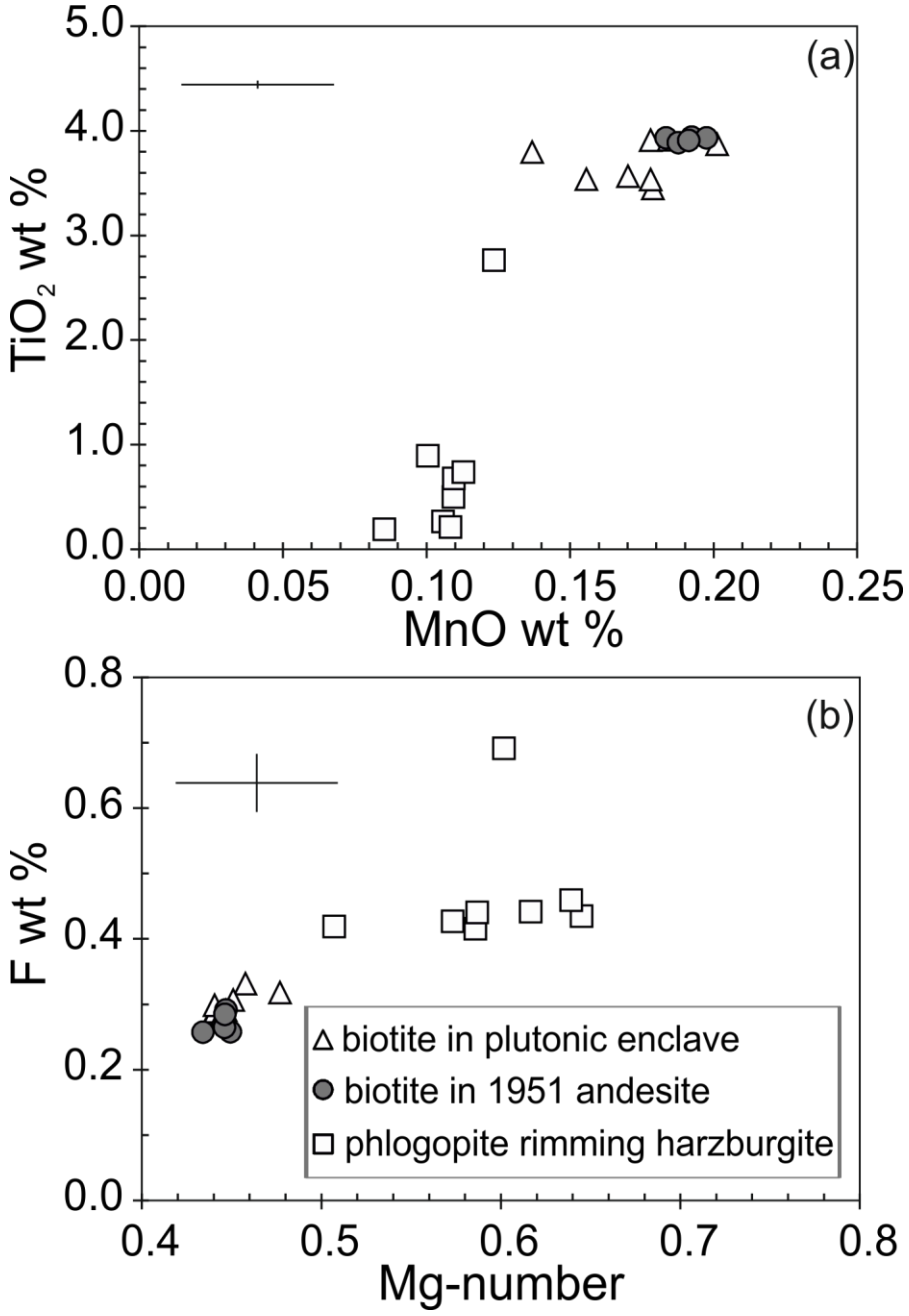
(a)
5.0
4.0
3.0
2.0
1.0
0.0
TiO2 wt %
0.00
0.05
0.10
0.15
0.20
0.25
MnO wt %
(b)
0.8
0.6
0.4
0.2
0.0
F wt %
0.4
0.5
0.6
0.7
0.8
Mg-number
biotite in plutonic enclave
biotite in 1951 andesite
phlogopite rimming harzburgite

Fig. 12

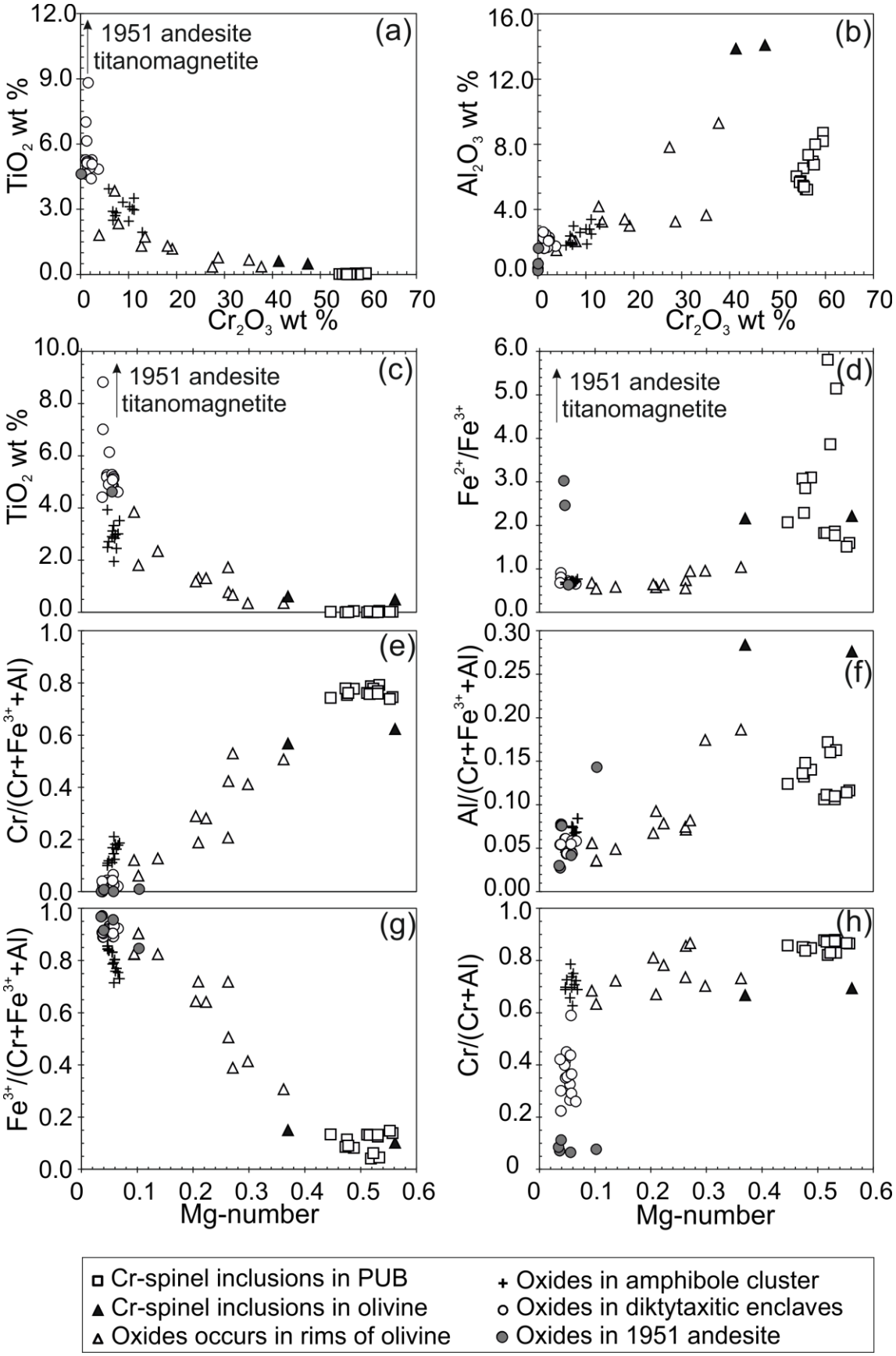
(a)
1951 andesite
titanomagnetite
TiO2 wt %
Cr2O3 wt %
(b)
Al2O3 wt %
Cr2O3 wt %
(c)
1951 andesite
titanomagnetite
TiO2 wt %
(d)
1951 andesite
titanomagnetite
Fe2+/Fe3+
(e)
Cr/(Cr+Fe3++Al)
(f)
Al/(Cr+Fe3++Al)
(g)
Fe3+/(Cr+Fe3++Al)
Mg-number
(h)
Cr/(Cr+Al)
Mg-number
Cr-spinel inclusions in PUB
Cr-spinel inclusions in olivine
Oxides occurs in rims of olivine
Oxides in amphibole cluster
Oxides in diktytaxitic enclaves
Oxides in 1951 andesite

Fig. 13

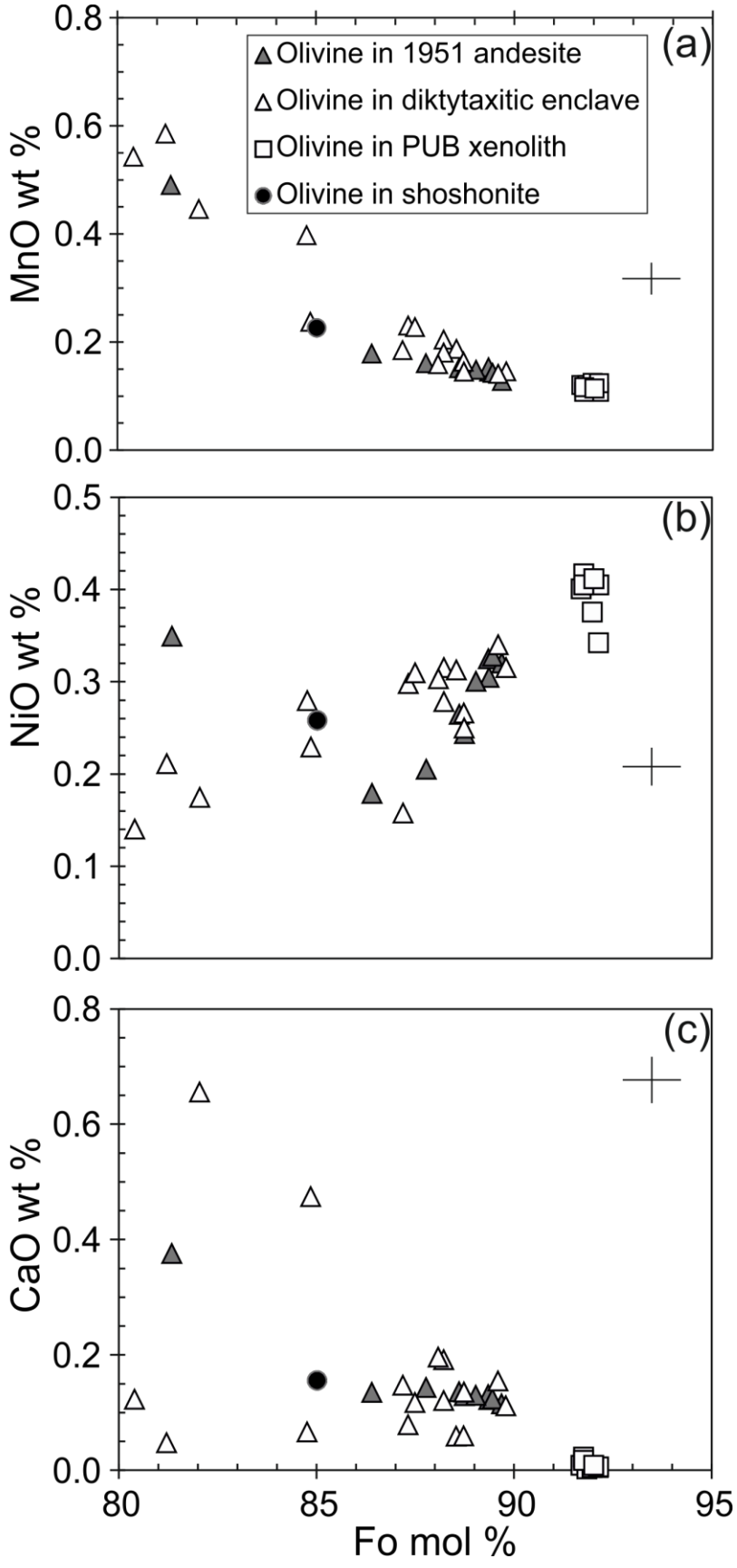
Olivine in 1951 andesite
Olivine in diktytaxitic enclave
Olivine in PUB xenolith
Olivine in shoshonite
(a)
(b)
(c)
MnO wt %
NiO wt %
CaO wt %
Fo mol %
0.0
0.2
0.4
0.6
0.8
0.1
0.3
0.5
80
85
90
95

Fig. 14

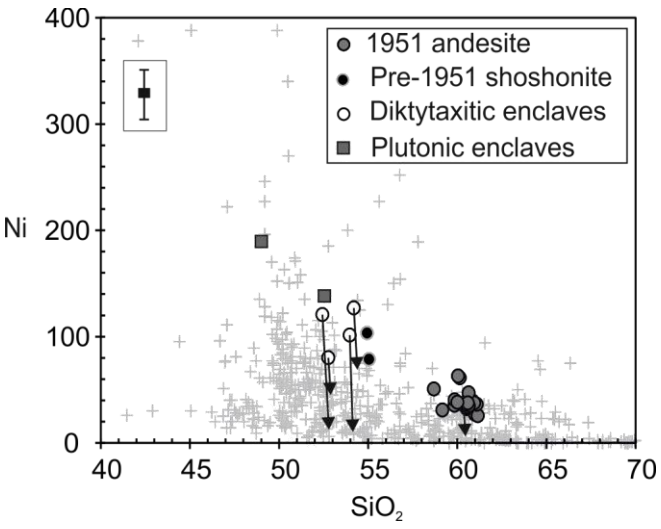
1951 andesite
Pre-1951 shoshonite
Diktytaxitic enclaves
Plutonic enclaves
Ni
SiO2
400
300
200
100
0
40
45
50
55
60
65
70

Fig. 15

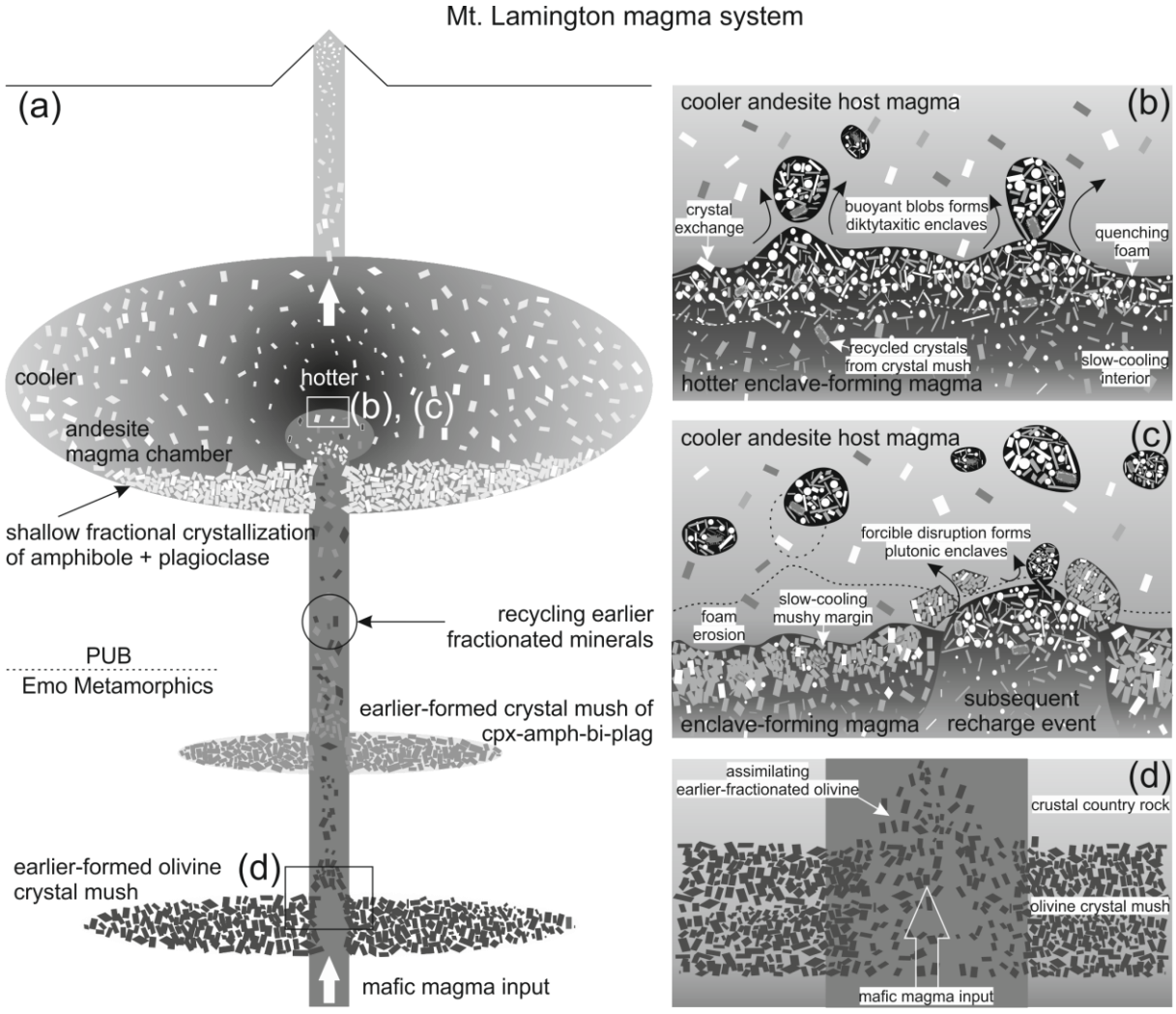
Mt. Lamington magma system
(a)
cooler
hotter
(b), (c)
andesite
magma chamber
shallow fractional crystallization
of amphibole + plagioclase
recycling earlier
fractionated minerals
PUB
Emo Metamorphics
earlier-formed crystal mush of
cpx-amph-bi-plag
earlier-formed olivine
crystal mush
(d)
mafic magma input
cooler andesite host magma
(b)
crystal
exchange
buoyant blobs forms
diktytaxitic enclaves
quenching
foam
recycled crystals
from crystal mush
slow-cooling
interior
hotter enclave-forming magma
cooler andesite host magma
(c)
forcible disruption forms
plutonic enclaves
foam
erosion
slow-cooling
mushy margin
subsequent
recharge event
enclave-forming magma
assimilating
earlier-fractionated olivine
(d)
crustal country rock
olivine crystal mush
mafic magma input

Fig. 16

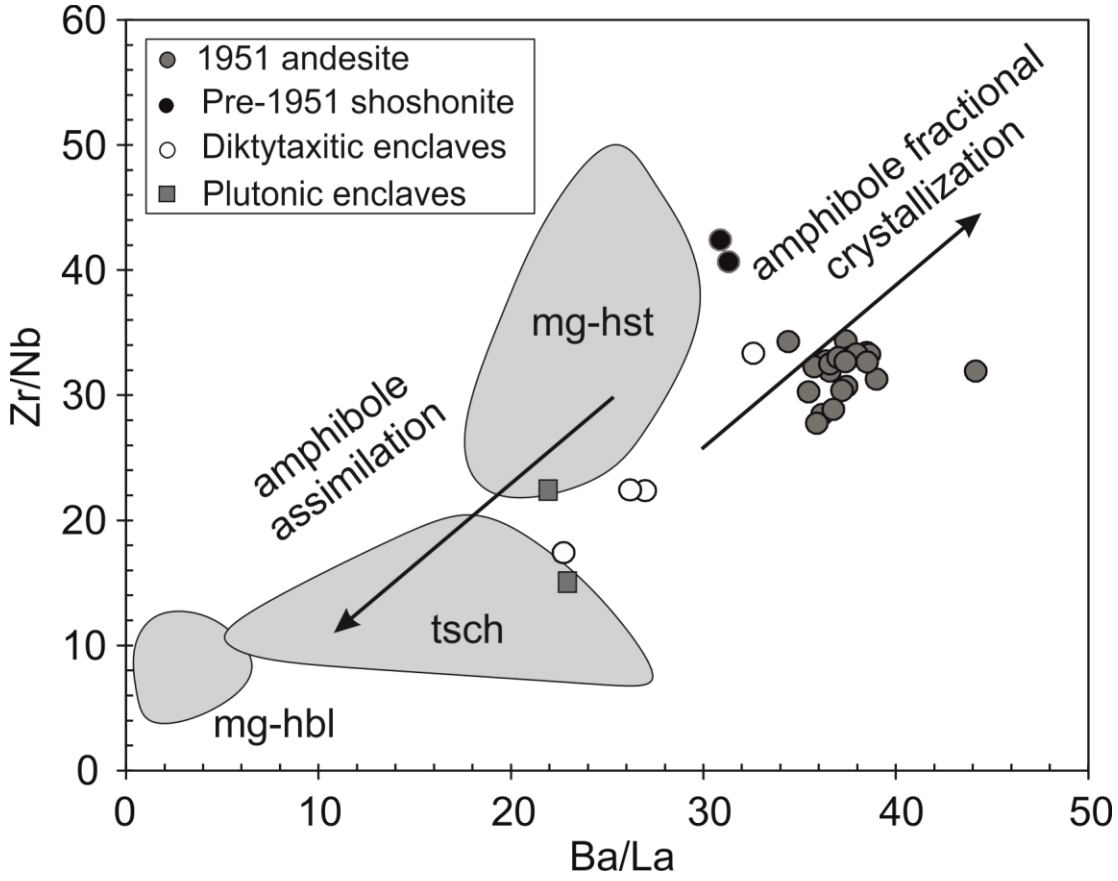
1951 andesite
Pre-1951 shoshonite
Diktytaxitic enclaves
Plutonic enclaves
mg-hst
tsch
mg-hbl
amphibole fractional crystallization
amphibole assimilation
Zr/Nb
Ba/La
0
10
20
30
40
50
60

Fig. 17

Table 1: Major and trace element and Sr-Nd isotopic compositions of samples from Mt. Lamington, Papua New Guinea

	1951 Andesite								
Samples	LAM-2	LAM-3	LAM-4	LAM-5	LAM-6H	LAM-8H	LAM-9H	LAM-10H	LAM-11
SiO_2	*61.00*	*60.65*	*60.54*	*61.15*	*60.02*	*61.10*	*60.66*	*60.86*	*60.49*
TiO_2	*0.63*	*0.61*	*0.65*	*0.64*	*0.61*	*0.63*	*0.63*	*0.63*	*0.60*
Al_2O_3	*17.29*	*17.31*	*16.97*	*17.30*	*17.22*	*17.19*	*17.03*	*17.16*	*17.35*
FeO_{tot}	*5.15*	*4.97*	*5.53*	*5.28*	*5.04*	*5.23*	*5.35*	*5.37*	*4.85*
MnO	*0.10*	*0.11*	*0.11*	*0.11*	*0.11*	*0.10*	*0.10*	*0.10*	*0.11*
MgO	*2.86*	*3.24*	*3.30*	*2.94*	*3.38*	*3.09*	*3.13*	*3.05*	*3.31*
CaO	*5.71*	*5.76*	*5.84*	*5.71*	*5.90*	*5.56*	*5.80*	*5.70*	*5.66*
Na_2O	*4.50*	*4.43*	*4.44*	*4.53*	*4.46*	*4.45*	*4.47*	*4.45*	*4.49*
K_2O	*2.18*	*2.14*	*2.15*	*2.16*	*2.10*	*2.14*	*2.17*	*2.18*	*2.14*
P_2O_5	*0.23*	*0.24*	*0.23*	*0.22*	*0.23*	*0.17*	*0.26*	*0.24*	*0.25*
Total	*99.66*	*99.46*	*99.75*	*100.04*	*99.07*	*99.67*	*99.58*	*99.74*	*99.25*
Cr	70	74	89	64	94	96	109	98	73
Ni	27	47	32	25	37	36	43	40	35
Co	33	57	36	40	32	31	37	37	30
Cu	17	17	13	13	18	12	14	23	13
Ga	20	20	20	20	19	20	20	20	20
Sc	11.8	12.5	13.5	13.1	12.7	11.7	12.4	12.8	13.3
V	99	105	114	102	121	107	112	110	115
Cs	2.45	2.49	2.74	2.51	2.62	2.73	2.72	2.56	2.58
Rb	52.7	52.6	55.9	55.0	53.6	52.9	54.2	54.0	55.9
Ba	664	650	622	621	690	650	656	639	660
Sr	997	922	965	940	942	934	985	926	881
Th	4.21	4.19	4.03	4.01	4.86	4.81	4.44	4.26	4.44
U	1.23	1.12	1.09	1.12	1.26	1.36	1.22	1.24	1.28
Pb	15.72	15.40	14.64	14.75	15.54	15.79	15.62	15.77	15.72
Nb	4.78	5.42	5.25	5.47	5.07	5.02	4.91	5.14	5.34
Zr	*164*	*154*	*164*	*168*	*154*	*160*	*162*	*164*	*154*
Y	15.70	15.81	16.48	15.81	17.43	15.01	15.96	16.49	16.88
La	17.76	17.96	15.96	16.59	18.55	14.72	17.41	17.46	17.97
Ce	36.54	36.85	33.18	34.05	38.34	30.13	36.05	36.28	37.23
Pr	5.06	5.00	4.70	4.64	5.20	4.13	5.02	5.00	5.10
Nd	20.31	19.95	19.01	18.56	20.66	16.73	20.23	19.93	20.31
Sm	3.95	3.86	3.75	3.62	4.03	3.38	3.95	3.88	3.95
Eu	1.17	1.13	1.11	1.06	1.15	1.06	1.17	1.14	1.14
Gd	4.07	3.70	3.87	3.53	3.69	3.32	4.13	3.80	3.79
Tb	0.51	0.49	0.49	0.45	0.52	0.44	0.52	0.49	0.51
Dy	2.72	2.66	2.58	2.44	2.81	2.43	2.74	2.65	2.74
Ho	0.54	0.52	0.52	0.48	0.55	0.48	0.55	0.54	0.53
Er	1.40	1.36	1.34	1.27	1.47	1.28	1.41	1.38	1.42
Tm	0.23	0.22	0.22	0.21	0.24	0.21	0.23	0.23	0.23
Yb	1.38	1.33	1.34	1.23	1.45	1.29	1.40	1.35	1.39
Lu	0.22	0.21	0.21	0.20	0.23	0.21	0.22	0.21	0.22
$^{87}Sr/^{86}Sr$	0.703968	0.703914	0.703802	0.703875	0.703953	0.703922	0.703881	0.703832	0.703952
$^{143}Nd/^{144}Nd$	0.512852	0.512871	0.512851	0.512894	0.512866	0.512876	0.512870	0.512856	0.512854

I in the column headings refers to the enclave sample separated from the corresponding andesite host sample (H).

Italic **data are from Arculus et al. (1983), as well as unpublished data; non-Italic trace element/Mn data are derived from ICP-MS analysis at Durham University.**

Two batches of ICP-MS analysis were carried out, LAM-1, -6H, -8I, -13, -27A and -27D were analyzed in batch 1, and the rest were analyzed in batch 2.

Multiple analyses of W2 and BHVO-1 standards are shown as averaged values and relative standard deviations (values in brackets); S value refers to standard error of W2, BHVO-1 and AGV-1 regression line.

Sr-Nd isotope compositions are analyzed at UCLA (SRM987 $^{87}Sr/^{86}Sr = 0.710248 \pm 17$; La Jolla $^{143}Nd/^{144}Nd = 0.511840 \pm 11$).

LAM-6I, -10I, -21I are plutonic enclaves; LAM-19I, -20I are intermediate enclaves; the rest of the magmatic enclaves are diktytaxitic enclaves.

Table 1: continued

Samples	LAM-13	LAM-14	LAM-17	LAM-19H	LAM-20H	LAM-21H	LAM-22H	LAM-23	LAM-24
SiO_2	*60.66*	*58.70*	*60.95*	*60.54*	*60.57*	*59.85*		*59.86*	*60.52*
TiO_2	*0.61*	*0.66*	*0.63*	*0.65*	*0.65*	*0.65*		*0.63*	*0.65*
Al_2O_3	*17.47*	*16.98*	*17.27*	*17.03*	*17.14*	*16.98*		*17.19*	*17.24*
FeO_{tot}	*4.98*	*5.41*	*5.35*	*5.49*	*5.43*	*5.52*		*5.36*	*5.40*
MnO	*0.11*	*0.12*	*0.10*	*0.11*	*0.11*	*0.11*	0.10	*0.11*	*0.10*
MgO	*3.16*	*4.07*	*3.03*	*3.27*	*3.23*	*3.44*		*3.32*	*3.26*
CaO	*5.81*	*6.37*	*5.70*	*5.79*	*5.86*	*5.92*		*5.98*	*5.83*
Na_2O	*4.42*	*4.24*	*4.47*	*4.41*	*4.45*	*4.38*		*4.45*	*4.44*
K_2O	*2.13*	*2.12*	*2.19*	*2.16*	*2.14*	*2.11*		*2.12*	*2.15*
P_2O_5	*0.25*	*0.24*	*0.26*	*0.28*	*0.24*	*0.25*		*0.22*	*0.23*
Total	*99.60*	*98.91*	*99.96*	*99.73*	*99.80*	*99.19*		*99.24*	*99.81*
Cr	82	126	92	110	91	108	252	108	104
Ni	35	51	38	39	33	35	33	40	36
Co	43	65	38	36	30	37	15	33	31
Cu	31	21	18	14	15	13	20	20	14
Ga	19	21	20	20	20	20	20	21	20
Sc	11.5	15.1	12.0	13.3	13.5	12.7	12.6	13.2	12.9
V	112	131	111	115	116	117	119	117	115
Cs	2.47	1.28	2.42	2.72	2.75	2.65	2.79	2.61	2.68
Rb	49.6	52.9	55.3	53.6	54.2	53.1	51.3	53.7	55.1
Ba	695	642	660	656	627	631	667	657	647
Sr	924	1002	1000	924	982	929	936	1031	1013
Th	5.02	3.98	4.28	4.86	4.39	4.63	4.94	4.45	4.49
U	1.32	1.13	1.25	1.28	1.24	1.23	1.30	1.12	1.16
Pb	16.45	31.15	15.58	16.28	14.76	15.00	16.53	15.56	15.39
Nb	4.74	4.63	5.09	4.99	4.95	4.99	4.46	4.85	4.93
Zr	*153*	*151*	*170*	*166*	*162*	*162*		*160*	*164*
Y	16.42	16.97	16.08	16.26	16.28	16.56	15.96	16.56	15.99
La	19.44	16.68	17.15	16.99	17.23	17.25	18.62	17.75	17.04
Ce	39.95	35.21	35.64	35.05	35.18	35.93	37.83	36.49	35.27
Pr	5.27	5.05	4.99	4.86	4.91	4.95	5.14	5.14	4.94
Nd	20.97	20.80	20.11	19.58	19.61	19.69	20.48	20.85	20.03
Sm	4.07	4.17	3.92	3.89	3.83	3.87	3.97	4.06	3.90
Eu	1.17	1.25	1.14	1.16	1.13	1.14	1.18	1.21	1.15
Gd	3.64	4.35	4.06	3.83	3.88	3.79	3.89	4.29	4.10
Tb	0.51	0.56	0.51	0.50	0.50	0.49	0.51	0.53	0.51
Dy	2.79	2.95	2.67	2.72	2.65	2.68	2.72	2.83	2.70
Ho	0.55	0.60	0.54	0.54	0.53	0.52	0.55	0.57	0.56
Er	1.45	1.53	1.39	1.42	1.38	1.39	1.42	1.47	1.40
Tm	0.24	0.25	0.22	0.23	0.22	0.23	0.23	0.24	0.23
Yb	1.43	1.52	1.37	1.42	1.37	1.40	1.40	1.44	1.38
Lu	0.23	0.24	0.22	0.22	0.22	0.22	0.22	0.23	0.22
$^{87}Sr/^{86}Sr$	0.703921	0.703931	0.703916	0.703919	0.703952	0.703902		0.703903	0.703923
$^{143}Nd/^{144}Nd$	0.512873	0.512837	0.512848	0.512879	0.512884	0.512853		0.512875	0.512860

Table 1: continued

					Magmatic Enclaves				
Samples	LAM-25	LAM-26	LAM-27A	LAM-27C	LAM-6I	LAM-7	LAM-8I	LAM-9I	LAM-10I
SiO_2	*60.60*	*60.01*	*59.17*	*60.14*	*52.57*	*52.77*	*53.97*		*49.01*
TiO_2	*0.65*	*0.61*	*0.67*	*0.61*	*0.90*	*0.93*	*0.95*		*1.07*
Al_2O_3	*17.22*	*17.06*	*17.37*	*17.24*	*14.46*	*16.01*	*15.50*		*14.06*
FeO_{tot}	*5.53*	*5.07*	*5.36*	*4.87*	*9.81*	*8.78*	*8.15*		*11.38*
MnO	*0.11*	*0.11*	*0.11*	*0.11*	0.24	0.18	0.14	0.16	0.24
MgO	*3.27*	*3.42*	*3.51*	*3.05*	*8.27*	*6.62*	*7.35*		*9.74*
CaO	*5.89*	*5.90*	*5.95*	*5.82*	*8.87*	*8.85*	*8.48*		*9.72*
Na_2O	*4.43*	*4.40*	*4.34*	*4.46*	*3.41*	*3.33*	*3.34*		*2.83*
K_2O	*2.14*	*2.10*	*2.17*	*2.14*	*1.34*	*1.52*	*1.48*		*1.07*
P_2O_5	*0.24*	*0.24*	*0.27*	*0.23*	*0.30*	*0.23*	*0.30*		*0.16*
Total	*100.08*	*98.92*	*98.92*	*98.67*	*100.17*	*99.22*	*99.66*		*99.27*
Cr	105	99	66	141	504	284	380	775	787
Ni	38	38	31	61	138	80	101	247	189
Co	32	90	55	69	67	51	64	42	111
Cu	17	15	20	20	26	45	47	72	317
Ga	21	20	19	19	20	20	19	18	20
Sc	13.1	13.4	12.7	13.1	26.1	26.7	21.9	31.9	31.3
V	119	110	120	113	193	202	196	240	258
Cs	2.70	2.67	2.45	2.15	1.18	1.71	1.72	1.58	0.80
Rb	55.2	52.5	48.0	52.8	29.9	32.1	30.2	28.4	18.7
Ba	652	636	693	654	420	383	471	351	302
Sr	1002	906	991	837	690	748	778	750	594
Th	4.43	4.91	5.47	3.89	1.94	3.00	4.10	2.24	1.08
U	1.13	1.25	1.56	1.08	0.60	0.88	1.12	0.65	0.32
Pb	15.42	15.59	16.27	14.38	8.02	9.40	11.40	6.95	5.97
Nb	4.90	5.09	4.82	5.37	5.90	5.29	6.27	3.10	4.66
Zr	*160*	*154*	*165*	*149*	*132*	*92*	*140*		*70*
Y	16.44	16.53	18.01	16.58	30.06	25.29	19.53	19.41	27.94
La	17.44	17.93	20.14	18.23	19.13	16.85	17.46	10.84	13.15
Ce	35.96	36.63	42.48	37.65	50.24	41.14	37.04	25.15	36.39
Pr	5.08	5.01	5.75	5.13	8.03	6.36	5.18	3.97	5.86
Nd	20.51	20.01	22.97	20.55	34.51	27.29	21.72	17.74	25.93
Sm	4.02	3.91	4.50	4.00	7.24	5.75	4.54	4.06	5.76
Eu	1.18	1.15	1.30	1.14	2.01	1.61	1.36	1.21	1.81
Gd	4.21	3.78	4.08	3.82	6.73	5.58	4.27	4.12	5.58
Tb	0.53	0.50	0.56	0.51	0.91	0.77	0.61	0.59	0.81
Dy	2.77	2.70	3.03	2.75	4.93	4.24	3.38	3.21	4.52
Ho	0.56	0.53	0.60	0.54	0.95	0.86	0.66	0.66	0.89
Er	1.42	1.42	1.58	1.40	2.51	2.24	1.71	1.68	2.40
Tm	0.23	0.23	0.26	0.23	0.41	0.36	0.27	0.27	0.39
Yb	1.41	1.42	1.56	1.38	2.51	2.23	1.63	1.63	2.39
Lu	0.22	0.23	0.25	0.21	0.39	0.35	0.26	0.25	0.38
$^{87}Sr/^{86}Sr$	0.703905	0.703914	0.703898	0.703909	0.703896	0.703899	0.703938		0.703925
$^{143}Nd/^{144}Nd$		0.512869	0.512895	0.512887	0.512816	0.512855	0.512853		0.512879

Table 1: continued

						Shoshonite		ICP-MS Standards		S
Samples	LAM-18	LAM-19I	LAM-20I	LAM-21I	LAM-22I	LAM-1	LAM-27D	W2	BHVO-1	
SiO_2	*52.45*				*54.20*	*55.06*	*54.95*			
TiO_2	*0.88*				*0.86*	*1.11*	*1.12*			
Al_2O_3	*15.65*				*15.30*	*15.99*	*16.43*			
FeO_{tot}	*8.42*				*8.48*	*6.31*	*6.08*			
MnO	0.14	0.28	0.25	0.17	0.20	*0.12*	*0.12*	0.18(5.24%)	0.18(6.97%)	
MgO	*8.15*				*6.84*	*5.89*	*5.24*			
CaO	*9.16*				*8.70*	*7.41*	*6.83*			
Na_2O	*3.32*				*3.44*	*3.44*	*3.47*			
K_2O	*1.40*				*1.69*	*3.17*	*3.33*			
P_2O_5	*0.27*				*0.25*	*0.64*	*0.63*			
Total	*99.85*				*99.98*	*99.14*	*98.20*			
Cr	448	840	1049	567	361	203	203	98(4.42%)	295(3.54%)	1.57%
Ni	121	1271	286	57	127	79	103	95(8.01%)	128(3.13%)	11.84%
Co	57	35	46	32	47	43	51	46(3.70%)	46(4.85%)	0.25%
Cu	33	24	138	23	45	42	45	106(4.63%)	141(3.83%)	0.17%
Ga	19	22	20	19	20	20	20	17.3(2.57%)	21.2(2.54%)	4.22%
Sc	29.5	31.6	31.7	28.3	23.3	20.5	18.0	36.2(2.14%)	31.8(2.60%)	2.14%
V	217	243	239	235	172	173	161	255(14.32%)	239(41.90%)	19.36%
Cs	1.43	1.61	0.85	1.96	1.69	1.52	1.81	0.94(8.47%)	0.13(32.68%)	3.14%
Rb	30.8	30.7	24.9	32.6	38.2	65.4	72.0	20.1(2.42%)	9.4(2.64%)	0.38%
Ba	386	375	348	400	492	952	927	167(1.81%)	132(2.58%)	0.22%
Sr	763	654	777	718	732	1315	1244	292(25.16%)	423(5.30%)	9.46%
Th	2.70	2.53	0.39	2.77	2.99	8.64	7.62	2.11(1.99%)	1.21(2.60%)	0.28%
U	0.80	0.73	0.13	0.77	0.87	2.33	2.09	0.48(1.23%)	0.41(1.46%)	0.98%
Pb	9.17	10.45	5.03	9.95	10.32	19.20	18.21	7.38(2.40%)	1.97(2.58%)	0.66%
Nb	3.72	5.22	4.14	4.01	5.18	9.45	9.55	7.47(2.29%)	19.17(1.34%)	1.51%
Zr	*124*				*116*	*384*	*405*			
Y	19.25	33.26	26.98	21.10	25.60	18.97	19.50	22.52(0.92%)	27.45(1.83%)	3.06%
La	11.83	13.37	12.58	13.26	18.79	30.40	30.02	10.07(2.79%)	15.03(2.68%)	1.20%
Ce	27.08	38.22	36.11	29.61	46.15	64.51	64.44	21.69(2.53%)	36.2(2.33%)	1.97%
Pr	4.13	6.69	6.07	4.51	7.03	8.56	8.61	3.10(0.75%)	5.64(0.76%)	1.39%
Nd	18.11	30.92	27.13	19.56	29.60	33.45	33.45	13.52(0.84%)	25.95(1.32%)	0.77%
Sm	4.03	7.10	6.01	4.34	5.97	5.95	5.97	3.33(1.27%)	6.26(1.53%)	1.44%
Eu	1.20	1.97	1.91	1.32	1.73	1.68	1.66	1.10(1.54%)	2.09(2.27%)	3.78%
Gd	4.00	6.98	5.90	4.55	5.74	5.09	5.13	3.69(3.11%)	6.30(5.11%)	12.23%
Tb	0.57	0.99	0.83	0.66	0.78	0.64	0.66	0.63(1.65%)	0.98(2.33%)	0.61%
Dy	3.15	5.43	4.54	3.62	4.27	3.35	3.44	3.82(0.92%)	5.33(1.60%)	1.53%
Ho	0.67	1.09	0.90	0.75	0.84	0.63	0.65	0.79(0.80%)	1.00(1.25%)	0.88%
Er	1.65	2.86	2.33	1.93	2.25	1.65	1.69	2.11(0.64%)	2.42(1.42%)	1.77%
Tm	0.27	0.47	0.37	0.31	0.37	0.26	0.27	0.35(0.59%)	0.36(1.84%)	4.30%
Yb	1.61	2.85	2.25	1.85	2.25	1.55	1.61	2.07(1.23%)	2.02(2.24%)	1.47%
Lu	0.26	0.44	0.35	0.28	0.36	0.25	0.26	0.33(1.03%)	0.30(1.09%)	3.73%
$^{87}Sr/^{86}Sr$	0.703871				0.703828	0.703683	0.703705			
$^{143}Nd/^{144}Nd$	0.512881				0.512887	0.512850	0.512860			

Table 2: Representative point counting results

	1951 andesite														
Sample	LAM-3			LAM-5			LAM-6H			LAM-9H			LAM-23		
Counts/prop./std.	n	%	σ	n	%	σ	n	%	σ	n	%	σ	n	%	σ
Olivine	2	0.7	*0.5*	0	0.0	*0.0*	5	1.7	*0.7*	1	0.3	*0.3*	9	1.1	*0.4*
Amphibole	54	18.0	*2.2*	59	19.7	*2.3*	79	26.3	*2.5*	73	24.3	*2.5*	172	21.5	*1.5*
Plagioclase	104	34.7	*2.7*	108	36.0	*2.8*	90	30.0	*2.6*	98	32.7	*2.7*	292	36.5	*1.7*
Oxides	4	1.3	*0.7*	8	2.7	*0.9*	3	1.0	*0.6*	4	1.3	*0.7*	26	3.3	*0.6*
Biotite	3	1.0	*0.6*	3	1.0	*0.6*	3	1.0	*0.6*	4	1.3	*0.7*	15	1.9	*0.5*
Clinopyroxene	0	0.0	*0.0*	0	0.0	*0.0*	0	0.0	*0.0*	0	0.0	*0.0*	0	0.0	*0.0*
Melt	112	37.3	*2.8*	101	33.7	*2.7*	99	33.0	*2.7*	112	37.3	*2.8*	268	33.5	*1.7*
Bubble	21	7.0	*1.5*	21	7.0	*1.5*	21	7.0	*1.5*	8	2.7	*0.9*	18	2.3	*0.5*
Total	300	100		300	100		300	100		300	100		800	100	
Bubble-free Crystallinity %		59.9			63.8			64.5			61.6			65.7	

The point counting does not differentiate phenocryst/antecryst/xenocryst;
In 1951 andesite and diktytaxitic enclaves, orthopyroxene countings are included in the olivine group;
Bubble-free crystallinity = 100(ol+amph+plag+ox+bi+cpx)/(ol+amph+plag+ox+bi+cpx+melt);
Standard deviation σ = (P(100-P)/N)0.5, where P = the proportion of each phase in percent, and N = the total counts, according to van der Plas & Tobi (1965).

Table 2: continued

	Diktytaxitic enclave												Intermediate			Plutonic enclave					
Sample	LAM-7			LAM-8I			LAM-9I			LAM-18			LAM-22I			LAM-19I			LAM-6I			LAM-10I		
Counts/prop./std.	n	%	σ	n	%	σ	n	%	σ	n	%	σ	n	%	σ	n	%	σ	n	%	σ	n	%	σ
Olivine	4	1.3	*0.7*	11	3.7	*1.1*	13	4.3	*1.2*	12	4.0	*1.1*	6	2.0	*0.8*	0	0.0	*0.0*	0	0.0	*0.0*	0	0.0	*0.0*
Amphibole	133	44.3	*2.9*	138	46.0	*2.9*	121	40.3	*2.8*	129	43.0	*2.9*	140	46.7	*2.9*	171	48.0	*2.6*	167	47.7	*2.7*	691	69.1	*1.5*
Plagioclase	62	20.7	*2.3*	77	25.7	*2.5*	80	26.7	*2.6*	78	26.0	*2.5*	94	31.3	*2.7*	81	22.8	*2.2*	127	36.3	*2.6*	217	21.7	*1.3*
Oxides	1	0.3	*0.3*	7	2.3	*0.9*	6	2.0	*0.8*	9	3.0	*1.0*	0	0.0	*0.0*	3	0.8	*0.5*	4	1.1	*0.6*	10	1.0	*0.3*
Biotite	1	0.3	*0.3*	0	0.0	*0.0*	0	0.0	*0.0*	0	0.0	*0.0*	4	1.3	*0.7*	3	0.8	*0.5*	7	2.0	*0.7*	9	0.9	*0.3*
Clinopyroxene	0	0.0	*0.0*	0	0.0	*0.0*	6	2.0	*0.8*	23	7.7	*1.5*	0	0.0	*0.0*	0	0.0	*0.0*	0	0.0	*0.0*	0	0.0	*0.0*
Melt	58	19.3	*2.3*	50	16.7	*2.2*	25	8.3	*1.6*	8	2.7	*0.9*	45	15.0	*2.1*	49	13.8	*1.8*	17	4.9	*1.1*	24	2.4	*0.5*
Bubble	41	13.7	*2.0*	17	5.7	*1.3*	49	16.3	*2.1*	41	13.7	*2.0*	11	3.7	*1.1*	49	13.8	*1.8*	28	8.0	*1.5*	49	4.9	*0.7*
Total	300	100		300	100		300	100		300	100		300	100		356	100		350	100		1000	100	
Bubble-free Crystallinity %		77.6			82.3			90.0			96.9			84.4			84.0			94.7			97.5	

Table 3: Representative amphibole compositions

	1951 andesite						Diktytaxitic enclave							Plutonic enclave		Shoshonite		PUB dunite		
Type	unzoned		normal-zoned		reverse-zoned		phenocryst-like			acicular		ol-rimming		amph cluster		phenocryst		amph rim		1 σ
Sample	LAM-10-0023		LAM-23-0001		LAM-23-0002		LAM-8I-0011			LAM-8I-0010		LAM-8I-0015		LAM-10I-0008		LAM-27D-0050		LAM-23		error
Analysis	27/1.	29/1.	37/1.	38/1.	27/1.	28/1.	14/1.	15/1.	16/1.	2/1.	4/1.	21/1.	23/1.	4/1.	5/1.	50/1.	51/1.	9/1.	13/1.	
Position	core	core	core	rim	core	rim	core	inner	outer	core	core	core	core	core	core	core	core	core	core	
SiO_2	47.70	42.96	42.94	44.68	45.43	41.90	44.84	41.57	41.82	42.76	42.98	42.30	42.35	45.92	43.66	41.79	40.73	47.24	48.46	0.57
TiO_2	1.20	2.07	1.88	1.55	1.45	2.13	1.49	2.33	2.22	1.50	0.96	2.24	2.00	1.09	1.60	2.67	3.53	1.27	0.82	0.03
Al_2O_3	7.54	11.12	11.81	9.20	8.90	13.11	9.83	13.09	12.92	12.95	12.64	13.25	11.72	9.25	11.22	12.86	13.43	8.91	6.37	0.49
Cr_2O_3	0.01	0.04	0.13	0.01	0.01	0.06	0.03	0.03	0.01	0.01	0.00	0.04	0.00	0.66	0.09	0.30	0.05	0.00	0.25	0.02
FeO	13.59	15.41	12.85	14.82	14.87	10.49	14.03	10.86	11.09	11.44	11.27	11.38	13.64	13.34	14.57	8.97	9.99	13.57	12.71	0.28
MgO	14.17	12.49	13.65	12.98	13.30	15.01	13.39	14.79	15.00	14.91	15.04	14.27	12.86	13.80	12.39	15.45	15.04	13.79	15.23	0.16
CaO	11.37	11.24	11.77	11.31	11.49	12.04	11.59	12.21	11.90	11.79	11.86	12.03	11.78	11.43	11.34	11.87	11.66	11.02	11.45	0.28
MnO	0.38	0.38	0.27	0.42	0.41	0.12	0.35	0.15	0.13	0.15	0.18	0.14	0.28	0.36	0.32	0.10	0.11	0.39	0.44	0.01
Na_2O	1.54	2.23	2.25	1.89	1.81	2.47	2.05	2.56	2.48	2.47	2.51	2.49	2.21	1.71	2.09	2.57	2.50	1.96	1.59	0.13
K_2O	0.52	0.77	0.73	0.62	0.62	0.66	0.66	0.67	0.63	0.61	0.52	0.67	0.67	0.44	0.71	1.30	1.00	0.86	0.41	0.23
F	0.15	0.17	0.18	0.18	0.15	0.15	0.10	0.14	0.15	0.17	0.14	0.15	0.14	0.19	0.16	0.32	0.19	0.24	0.17	0.05
Cl	0.05	0.06	0.01	0.07	0.06	0.02	0.05	0.01	0.02	0.02	0.01	0.01	0.04	0.03	0.05	0.01	0.01	0.06	0.04	0.01
Total	98.22	98.99	98.47	97.74	98.51	98.17	98.43	98.42	98.41	98.82	98.14	98.99	97.72	98.24	98.24	98.23	98.28	99.31	97.95	
TSi	6.866	6.241	6.224	6.542	6.589	6.035	6.509	6.002	6.009	6.103	6.168	6.073	6.221	6.619	6.371	6.050	5.875	6.754	6.962	
TAl(IV)	1.134	1.759	1.776	1.458	1.411	1.965	1.491	1.998	1.991	1.897	1.832	1.927	1.779	1.381	1.629	1.950	2.125	1.246	1.038	
Total	8.00	8.00	8.00	8.00	8.00	8.00	8.00	8.00	8.00	8.00	8.00	8.00	8.00	8.00	8.00	8.00	8.00	8.00	8.00	
M1-3 Al(VI)	0.146	0.145	0.241	0.130	0.111	0.262	0.190	0.229	0.197	0.281	0.306	0.316	0.251	0.190	0.301	0.244	0.158	0.256	0.040	
M1-3 Ti	0.130	0.227	0.205	0.171	0.158	0.230	0.163	0.253	0.240	0.161	0.104	0.242	0.221	0.119	0.175	0.290	0.383	0.137	0.088	
M1-3 Cr	0.002	0.005	0.015	0.001	0.001	0.007	0.003	0.004	0.002	0.002	0.000	0.005	0.000	0.075	0.011	0.034	0.005	0.000	0.028	
M1-3 Fe^{3+}	0.696	0.886	0.686	0.785	0.785	0.709	0.669	0.643	0.841	0.889	0.877	0.606	0.622	0.787	0.693	0.444	0.708	0.644	0.749	
M1-3 Mg	3.041	2.705	2.949	2.832	2.876	3.223	2.898	3.184	3.213	3.173	3.217	3.055	2.816	2.965	2.695	3.334	3.235	2.938	3.262	
M1-3 Fe^{2+}	0.940	0.986	0.871	1.029	1.019	0.555	1.035	0.668	0.491	0.476	0.475	0.760	1.054	0.820	1.085	0.642	0.497	0.978	0.778	
M1-3 Mn	0.047	0.046	0.033	0.052	0.051	0.015	0.043	0.019	0.016	0.018	0.022	0.017	0.035	0.044	0.040	0.012	0.014	0.047	0.054	
Total	5.00	5.00	5.00	5.00	5.00	5.00	5.00	5.00	5.00	5.00	5.00	5.00	5.00	5.00	5.00	5.00	5.00	5.00	5.00	
M4 Ca	1.753	1.749	1.828	1.774	1.786	1.858	1.803	1.889	1.832	1.804	1.824	1.851	1.854	1.766	1.774	1.842	1.802	1.687	1.763	
M4 Na	0.247	0.251	0.172	0.226	0.214	0.142	0.197	0.111	0.168	0.196	0.176	0.149	0.146	0.234	0.226	0.158	0.198	0.313	0.237	
Total	2.00	2.00	2.00	2.00	2.00	2.00	2.00	2.00	2.00	2.00	2.00	2.00	2.00	2.00	2.00	2.00	2.00	2.00	2.00	
A Na	0.183	0.377	0.460	0.311	0.297	0.548	0.379	0.604	0.523	0.487	0.522	0.544	0.483	0.245	0.366	0.564	0.502	0.229	0.206	
A K	0.095	0.143	0.136	0.117	0.114	0.120	0.122	0.123	0.116	0.112	0.095	0.122	0.126	0.080	0.133	0.241	0.183	0.156	0.074	
Total	0.278	0.521	0.596	0.427	0.411	0.669	0.502	0.727	0.639	0.599	0.617	0.666	0.609	0.325	0.499	0.805	0.685	0.386	0.281	
Classification	Mg-Hbl	Mg-Hst	Mg-Hst	Mg-Hbl	Mg-Hbl	Mg-Hst	Mg-Hbl	Mg-Hst	Mg-Hst	Mg-Hst	Mg-Hst	Mg-Hst	Mg-Hst	Mg-Hbl	Tsch-Prg	Mg-Hst	Mg-Hst	Mg-Hbl	Mg-Hbl	

normal-zoned - high Al core and low Al rim; reverse-zoned - low Al core and high Al rim; inner - inner rim; outer - outer rim; Classification is based on the nomentclature of Leake et al. (1997).

Table 4: Representative plagioclase compositions

	1951 andesite									Diktytaxitic enclave					Plutonic enclave			Shoshonite			
Type	Oscillatory		Sieve-textured			Patchy-zoned				Normal-zoned		Patchy-zoned			Oscillatory			Oscillatory			1 σ
Sample	LAM-23-0002		LAM-23-0009			LAM-23-0013				LAM-8I-0010		LAM-8I-0014			LAM-10I-0008			LAM-27D-0050			error
Analysis	29/1.	30/1.	49/1.	50/1.	51/1.	67/1.	69/1.	71/1.	73/1.	11/1.	12/1.	66/1.	67/1.	69/1.	17/1.	19/1.	20/1.	58/1.	59/1.	60/1.	
Position	core	rim	core	inner	outer	bright	dark	inner	outer	core	rim	bright	dark	rim	core	inner	outer	core	inner	outer	
SiO_2	55.33	60.12	56.39	52.95	58.06	57.35	58.77	56.52	59.54	53.99	59.91	49.69	63.57	57.81	57.12	59.77	61.35	54.29	55.46	58.91	0.14
Al_2O_3	27.59	24.59	27.67	29.70	26.13	26.48	25.91	27.72	25.69	28.05	24.15	30.78	22.22	26.84	27.54	25.36	24.90	28.05	27.62	24.95	0.16
FeO	0.24	0.24	0.22	0.48	0.32	0.20	0.20	0.18	0.19	0.42	0.25	0.44	0.54	0.33	0.24	0.27	0.29	0.22	0.21	0.23	0.001
CaO	10.48	6.69	9.93	12.53	8.22	8.91	8.00	10.15	7.10	10.99	6.71	14.69	5.93	8.88	9.42	7.05	6.51	11.10	10.56	7.56	0.03
SrO	0.38	0.26	0.39	0.28	0.25	0.27	0.30	0.27	0.22	0.32	0.21	0.26	0.18	0.30	0.32	0.25	0.24	0.43	0.38	0.27	0.003
Na_2O	5.55	7.62	5.93	4.41	6.82	6.64	7.12	6.04	7.30	5.39	7.63	3.49	7.10	6.35	6.34	7.42	7.77	5.17	5.51	7.04	0.05
K_2O	0.23	0.50	0.24	0.17	0.39	0.35	0.38	0.26	0.45	0.20	0.60	0.11	1.47	0.29	0.30	0.44	0.48	0.22	0.32	0.80	0.004
Total	99.82	100.01	100.78	100.61	100.22	100.19	100.69	101.16	100.50	99.41	99.48	99.47	101.17	100.82	101.30	100.56	101.55	99.50	100.10	99.77	
Si	2.502	2.683	2.520	2.389	2.596	2.566	2.612	2.513	2.647	2.452	2.687	2.276	2.825	2.578	2.533	2.656	2.697	2.468	2.502	2.643	
Al	1.470	1.294	1.457	1.579	1.377	1.396	1.357	1.453	1.346	1.501	1.277	1.662	1.164	1.411	1.439	1.328	1.290	1.502	1.468	1.319	
Fe	0.009	0.009	0.008	0.018	0.012	0.007	0.007	0.007	0.007	0.016	0.009	0.017	0.020	0.012	0.009	0.010	0.011	0.009	0.008	0.009	
Ca	0.508	0.320	0.476	0.606	0.394	0.427	0.381	0.483	0.338	0.535	0.323	0.721	0.282	0.424	0.448	0.336	0.307	0.541	0.510	0.363	
Na	0.487	0.659	0.514	0.386	0.591	0.576	0.613	0.521	0.629	0.474	0.664	0.310	0.612	0.549	0.545	0.639	0.662	0.456	0.482	0.613	
K	0.013	0.028	0.014	0.010	0.022	0.020	0.021	0.015	0.025	0.011	0.034	0.006	0.083	0.017	0.017	0.025	0.027	0.013	0.018	0.046	
Sr	0.010	0.007	0.010	0.007	0.007	0.007	0.008	0.007	0.006	0.008	0.005	0.007	0.005	0.008	0.008	0.006	0.006	0.011	0.010	0.007	
Total	4.999	5.000	4.999	4.996	4.999	5.000	4.999	4.999	5.000	4.997	4.999	4.999	4.991	4.999	4.999	4.999	4.999	4.999	4.998	4.999	
An	50.4	31.8	47.4	60.5	39.1	41.7	37.5	47.4	34.1	52.4	31.6	69.5	28.9	42.8	44.3	33.6	30.8	53.6	50.5	35.6	
Ab	48.3	65.4	51.2	38.5	58.7	56.3	60.4	51.1	63.4	46.5	65.0	29.9	62.6	55.5	54.0	64.0	66.5	45.2	47.7	60.0	
Or	1.3	2.8	1.4	1.0	2.2	2.0	2.1	1.5	2.5	1.1	3.4	0.6	8.5	1.7	1.7	2.5	2.7	1.3	1.8	4.5	

bright - bright core; dark - dark core; inner - inner rim; outer - outer rim; total iron displayed as Fe^{2+}; An = 100Ca/(Ca+Na+K); Ab = 100Na/(Ca+Na+K); Or = 100K/(Ca+Na+K).

Table 5: Representative mica compositions

	1951 andesite		Plutonic enclave		PUB rim		1 σ error
Sample	LAM23		LAM-10I		LAM-12		
Analysis	17-13	30-19	16-53	16-57	29	30	
SiO_2	37.36	37.55	37.30	37.29	39.20	39.78	0.54
TiO_2	3.93	3.94	3.80	3.87	0.50	0.68	0.04
Al_2O_3	14.47	13.93	14.45	14.65	14.33	13.50	0.57
Cr_2O_3	0.02	0.03	0.05	0.02	0.12	0.15	0.02
FeO	16.02	15.24	14.51	15.58	11.58	11.51	0.28
MgO	14.71	14.90	15.84	14.71	19.60	19.56	0.17
MnO	0.18	0.19	0.14	0.20	0.11	0.11	0.01
Na_2O	0.90	0.90	0.90	0.92	1.11	0.57	0.10
K_2O	8.69	8.63	9.00	8.85	8.65	9.20	0.43
F	0.26	0.26	0.32	0.29	0.42	0.44	0.05
Cl	0.11	0.10	0.07	0.11	0.07	0.07	0.01
Total	96.64	95.72	96.39	96.53	95.69	95.62	
T Si	5.549	5.611	5.529	5.542	5.741	5.836	
T Al(IV)	2.451	2.389	2.471	2.458	2.259	2.164	
Total	8.000	8.000	8.000	8.000	8.000	8.000	
M1-3 Al(VI)	0.081	0.065	0.054	0.108	0.214	0.170	
M1-3 Ti	0.439	0.442	0.423	0.433	0.055	0.075	
M1-3 Cr	0.002	0.004	0.006	0.002	0.013	0.017	
M1-3 Fe	1.990	1.905	1.798	1.937	1.419	1.412	
M1-3 Mg	3.257	3.319	3.500	3.260	4.280	4.278	
M1-3 Mn	0.023	0.024	0.017	0.025	0.014	0.014	
Total	5.792	5.759	5.799	5.765	5.994	5.965	
Na	0.259	0.260	0.258	0.266	0.314	0.162	
K	1.647	1.646	1.702	1.678	1.616	1.723	
Total	1.906	1.906	1.960	1.945	1.930	1.885	
Mg-number	0.43	0.45	0.48	0.44	0.59	0.59	

total iron displayed as Fe^{2+}; Mg-number = Mg/(Mg+Fe).

Table 6: Representative oxides compositions

	1951 andesite			Diktytaxitic enclave							Plutonic enclave				PUB xenoliths				Shoshonite	1 σ error
Type	Phenocryst		Cr-sp in ol	Microhenocryst		Reaction rim phase of olivines				Cr-sp in ol	inclusion in amph cluster				Cr-sp inclusions				Phenocryst	
Sample	LAM-23		LAM-23	LAM-8H		LAM-8I				LAM-8I	LAM-10I				LAM-23		LAM-12		LAM-27D	
Analysis	002-23	002-24	036-26	011-20	017-55	012-33	015-15	015-17	016-43	008-72	004-13	004-23	004-24	004-25	2	3	1	10	050-55	
SiO_2	0.06	0.09	0.11	0.08	0.10	0.08	0.11	0.09	0.08	0.15	0.08	0.08	0.08	0.10	0.06	0.08	0.06	0.18	0.06	0.001
TiO_2	32.26	4.61	0.49	4.84	4.41	0.77	0.35	2.34	1.30	0.61	3.93	3.12	2.71	1.94	0.02	0.05	0.02	0.02	31.87	0.02
Al_2O_3	0.25	1.61	14.08	1.74	2.07	3.25	9.30	2.04	3.39	13.87	1.79	1.88	1.83	3.08	6.53	6.94	8.71	6.04	0.66	0.006
Cr_2O_3	0.05	0.16	47.38	3.72	2.24	28.72	37.70	7.90	18.12	41.31	5.90	10.24	7.23	12.90	55.40	57.38	59.48	53.96	0.08	0.009
Fe_2O_3	4.69	58.70	8.08	53.97	54.26	36.04	23.99	53.72	43.46	11.43	52.91	50.37	53.89	45.96	8.80	6.38	3.27	10.18	6.03	0.08*
FeO	57.65	33.42	16.07	33.41	33.04	23.97	22.38	28.30	24.82	22.19	32.75	31.96	31.60	30.02	18.10	17.79	17.11	18.96	54.14	
MgO	1.32	1.12	11.55	1.13	0.72	4.81	7.13	2.52	4.01	7.31	0.90	1.06	0.91	1.04	9.21	9.51	10.33	8.57	3.49	0.001
CaO	0.00	0.02	0.01	0.04	0.13	0.04	0.02	0.15	0.11	0.09	0.04	0.01	0.07	0.14	0.00	0.00	0.00	0.00	0.01	0.01
MnO	0.48	0.66	0.28	0.65	0.57	0.86	0.79	0.58	0.72	0.48	0.64	0.70	0.63	0.59	0.33	0.32	0.35	0.43	0.29	0.001
NiO	0.01	0.02	0.16	0.04	0.02	0.21	0.14	0.20	0.22	0.06	0.06	0.06	0.06	0.04	0.08	0.08	0.04	0.14	0.01	0.001
Norm. total	96.77	100.42	98.21	99.61	97.55	98.75	101.91	97.83	96.24	97.51	98.99	99.48	99.03	95.83	98.52	98.53	99.37	98.46	96.64	
Si	0.002	0.003	0.004	0.003	0.004	0.003	0.004	0.003	0.003	0.005	0.003	0.003	0.003	0.004	0.002	0.003	0.002	0.006	0.002	
Ti	0.924	0.130	0.012	0.137	0.128	0.021	0.009	0.067	0.037	0.016	0.112	0.088	0.077	0.057	0.000	0.001	0.000	0.001	0.897	
Al	0.011	0.071	0.543	0.077	0.094	0.139	0.368	0.091	0.150	0.556	0.080	0.083	0.082	0.141	0.264	0.279	0.343	0.246	0.029	
Cr	0.001	0.005	1.226	0.111	0.068	0.826	1.001	0.237	0.539	1.111	0.177	0.305	0.217	0.396	1.504	1.549	1.570	1.476	0.002	
Fe^{3+}	0.134	1.657	0.199	1.531	1.575	0.986	0.606	1.532	1.231	0.293	1.512	1.428	1.540	1.342	0.227	0.164	0.082	0.265	0.170	
Fe^{2+}	1.836	1.048	0.440	1.053	1.065	0.729	0.629	0.897	0.781	0.631	1.040	1.007	1.003	0.974	0.520	0.508	0.478	0.548	1.695	
Mg	0.075	0.063	0.564	0.064	0.041	0.261	0.357	0.143	0.225	0.371	0.051	0.060	0.052	0.060	0.471	0.484	0.514	0.442	0.195	
Ca	0.000	0.001	0.000	0.001	0.006	0.002	0.001	0.006	0.004	0.003	0.002	0.000	0.003	0.006	0.000	0.000	0.000	0.000	0.000	
Mn	0.015	0.021	0.008	0.021	0.019	0.027	0.022	0.019	0.023	0.014	0.021	0.022	0.020	0.019	0.010	0.009	0.010	0.012	0.009	
Ni	0.000	0.001	0.004	0.001	0.001	0.006	0.004	0.006	0.007	0.002	0.002	0.002	0.002	0.001	0.002	0.002	0.001	0.004	0.000	
Total charge	7.866	6.343	7.801	6.469	6.425	7.014	7.394	6.468	6.769	7.707	6.488	6.572	6.460	6.658	7.773	7.836	7.918	7.735	7.830	
Mg-number	0.04	0.06	0.56	0.06	0.04	0.26	0.36	0.14	0.22	0.37	0.05	0.06	0.05	0.06	0.48	0.49	0.52	0.45	0.10	
Cr-number	0.11	0.06	0.69	0.59	0.42	0.86	0.73	0.72	0.78	0.67	0.69	0.79	0.73	0.74	0.85	0.85	0.82	0.86	0.07	

Fe_2O_3 wt % calculated from AB_2O_4 spinel stoichiometry; number of ions calculated on the basis of total cations = 3; Mg-number = Mg/(Mg+Fe^{2+}); Cr-number = 100Cr/(Cr+Al).

*** 1 σ error refers to analytical error of FeOtot as FeO.**

Table 7: Representative olivine compositions

	1951 andesite				Diktytaxitic enclave				PUB xenoliths		Shoshonite	
Type	Xenocryst				Xenocryst				Dunite ol		Phenocryst	1 σ
Sample	LAM-10H			LAM-23	LAM-8I				LAM-23		LAM-27D	error
Analysis	016-61	021-10	021-11	002-21	016-27	016-28	016-29	016-30	4	5	050-56	
Position	core	core	core	core	core		rim		random	random	core	
SiO_2	40.84	40.40	40.77	39.52	40.48	40.50	40.02	39.54	40.94	41.20	40.26	0.08
FeO_T	11.45	12.56	10.66	16.70	11.04	11.77	14.17	17.12	8.05	7.96	13.93	0.03
MnO	0.16	0.18	0.15	0.49	0.18	0.23	0.40	0.59	0.12	0.12	0.23	0.001
MgO	47.51	46.05	47.95	43.26	48.18	47.70	45.77	43.11	50.70	51.09	45.73	0.04
CaO	0.14	0.13	0.14	0.38	0.19	0.12	0.07	0.05	0.01	0.00	0.16	0.01
NiO	0.20	0.18	0.26	0.35	0.28	0.31	0.28	0.21	0.40	0.41	0.26	0.001
Total	100.36	99.56	100.00	100.78	100.44	100.67	100.75	100.65	100.23	100.79	100.64	
Si	1.006	1.010	1.005	0.995	0.994	0.996	0.994	0.998	0.993	0.993	1.001	
Fe	0.236	0.263	0.220	0.352	0.227	0.242	0.294	0.361	0.163	0.161	0.290	
Mn	0.003	0.004	0.003	0.010	0.004	0.005	0.008	0.013	0.002	0.002	0.005	
Mg	1.745	1.716	1.762	1.624	1.763	1.748	1.695	1.622	1.833	1.836	1.694	
Ca	0.004	0.004	0.004	0.010	0.005	0.003	0.002	0.001	0.000	0.000	0.004	
Ni	0.004	0.004	0.005	0.007	0.005	0.006	0.006	0.004	0.008	0.008	0.005	
Total	2.999	2.999	2.999	2.999	2.998	2.999	2.999	2.999	3.000	3.000	2.999	
Fo	87.8	86.4	88.6	81.3	88.2	87.5	84.8	81.2	91.7	91.8	85.0	

number of ions calculated on the basis of total cations = 3; total iron displayed as Fe^{2+}; Fo = 100Mg/(Mg+Fe).

Table 8: Representative pyroxene compositions

Type	Shoshonite		Diktytaxitic enclave				PUB		1 σ error	
	Cpx phenocryst		Cpx xenocryst		ol reaction rim phase (Opx)		PUB reaction rim phase (Opx)			
Sample	LAM-27D		LAM-18		LAM-8I		LAM-12		Cpx	Opx
Analysis	70	71	2	3	015-18	016-32	20	24		
SiO_2	51.62	51.30	53.15	51.23	55.96	55.89	54.09	55.67	0.08	0.09
TiO_2	0.68	0.80	0.27	0.49	0.08	0.06	0.02	0.01	0.004	0.001
Al_2O_3	2.99	3.19	1.85	3.64	0.36	0.51	3.86	0.20	0.006	0.003
Cr_2O_3	0.07	0.07	0.48	0.30	0.06	0.04	0.39	0.03	0.001	0.001
FeO	6.34	5.82	4.40	5.25	12.35	12.17	9.42	11.86	0.03	0.03
MnO	0.16	0.15	0.12	0.11	0.79	0.78	0.32	0.79	0.001	0.001
MgO	15.76	15.68	17.16	15.76	30.56	30.79	30.96	30.14	0.02	0.03
CaO	21.21	21.46	21.40	21.96	0.41	0.38	0.98	1.17	0.02	0.01
NiO	0.03	0.02	0.25	0.33	0.04	0.06	0.20	0.19	0.001	
Na_2O	0.35	0.35	0.01	0.01					0.001	
Total	99.22	98.85	99.09	99.08	100.61	100.69	100.26	100.05		
T Si	1.949	1.945	1.983	1.939	1.976	1.971	1.931	1.975		
T Al(IV)	0.051	0.055	0.017	0.061	0.007	0.011	0.069	0.004		
T Fe^{3+}	0.000	0.000	0.000	0.000	0.011	0.010	0.000	0.020		
total	2.000	2.000	2.000	2.000	1.994	1.992	2.000	2.000		
M1-2 Al(VI)	0.015	0.016	0.024	0.020	0.000	0.000	0.012	0.000		
M1-2 Ti	0.019	0.023	0.007	0.014	0.002	0.002	0.000	0.000		
M1-2 Cr	0.001	0.001	0.007	0.004	0.001	0.001	0.006	0.000		
M1-2 Fe^{3+}	0.000	0.000	0.000	0.000	0.000	0.000	0.000	0.010		
M1-2 Fe^{2+}	0.200	0.184	0.137	0.166	0.354	0.349	0.281	0.322		
M1-2 Mn	0.005	0.005	0.004	0.004	0.023	0.023	0.010	0.024		
M1-2 Mg	0.887	0.886	0.955	0.889	1.609	1.618	1.648	1.594		
M1-2 Ca	0.858	0.871	0.856	0.891	0.015	0.014	0.038	0.044		
M1-2 Na	0.013	0.013	0.009	0.012						
M1-2 Ni	0.001	0.000	0.000	0.000	0.001	0.002	0.006	0.005		
Total	2.000	2.000	2.000	2.000	2.006	2.008	2.000	2.000		
En	45.6	45.6	49.0	45.7	80.9	81.3	83.8	80.1		
Wo	44.1	44.9	43.9	45.8	0.8	0.7	1.9	2.2		
Fs	10.3	9.5	7.0	8.5	18.3	18.0	14.3	17.7		

number of ions calculated on the basis of 6 oxygen;

En = 100Mg/(Ca+Mg+Fe^{2+}); Wo = 100Ca/(Ca+Mg+Fe^{2+});

Fs = 100Fe^{2+}/(Ca+Mg+Fe_{2+}).

Table 9: Representative glass compositions

Sample	Diktytaxitic enclave				Plutonic enclave		1 σ error
	LAM-8I				LAM-10I		
Analysis	012-39	014-58	015-11	017-60	#28	#29	
SiO_2	75.93	77.76	76.08	73.29	78.27	76.96	0.43
Al_2O_3	13.01	13.13	13.14	15.90	12.56	12.96	0.16
Na_2O	3.12	2.61	3.31	5.05	2.16	2.27	0.06
MgO	0.07	0.03	0.07	0.04	0.09	0.07	0.01
K_2O	6.36	5.82	6.34	4.49	5.91	5.69	0.06
CaO	0.45	0.49	0.39	1.51	0.69	0.71	0.02
FeO	0.69	0.86	0.82	0.50	0.35	0.44	0.06
P_2O_5	0.02	0.02	0.02	0.02	0.02	0.01	0.01
TiO_2	0.16	0.13	0.13	0.11	0.11	0.12	0.001
MnO	0.03	0.04	0.03	0.01	0.01	0.02	0.001
Cl	0.12	0.15	0.09	0.04	0.01	0.01	0.01
F	0.02	0.00	0.00	0.01	0.00	0.01	0.01
Total	99.98	101.02	100.43	100.98	100.17	99.29	